

## Article

# In Situ LA-ICP-MS of Zoned Garnets from the Huanggang Skarn Iron–Tin Polymetallic Deposit, Southeastern Mongolia, Northern China

Wei Mei <sup>1</sup>, Banxiao Ruan <sup>1,\*</sup> and Hongyu Liu <sup>2</sup>

<sup>1</sup> The Institute of Geological Survey of China, University of Geosciences, Wuhan 430074, China; meiwei09@cug.edu.cn

<sup>2</sup> School of Earth Resources of China, University of Geosciences, Wuhan 430074, China; lhy@cug.edu.cn

\* Correspondence: bxruan@cug.edu.cn

**Abstract:** The Huanggang deposit is the most important and largest skarn Fe–Sn polymetallic deposit in the Southern Great Xing’an Range of Northeast China. Cassiterite, magnetite, and other metal minerals are related to the garnets within skarn systems. The zoned garnets from various skarn stages are able to record numerous geological and mineralizing processes including variations in physicochemical conditions and hydrothermal fluid evolution. In this contribution, we present the mineralogy, systematic major, trace, and rare earth element (REE) concentrations of zoned garnets from the Huanggang Fe–Sn polymetallic skarn deposit. The in situ analytical results of garnets in the prograde skarn stage from andradite core (Grt I) to grossular rim (Grt II) reveal that core sections were formed from a fluid that was generally LREE-rich, with relatively high  $\Sigma$ REE, high LREE/HREE ratios, and weak negative Eu anomalies, whereas rim sections were crystallized from a fluid that was typically HREE-rich, with relatively low  $\Sigma$ REE, low LREE/HREE ratios, and obviously negative Eu anomalies. The garnets of the retrograde skarn stage from Fe<sup>3+</sup>-rich andradite core (Grt III) to andradite rim (Grt IV) demonstrate that the core sections have a flat trend with high  $\Sigma$ REE and obvious negative Eu anomalies, whereas rim sections were formed from a fluid with relatively low  $\Sigma$ REE, HREE-rich and obviously negative Eu anomalies. The garnets from the prograde skarn stage principally display relatively lower U and higher Y and F concentrations than those from the retrograde skarn stage. Based on optical and textural characteristics, REE patterns, Eu anomalies, and trace element variations in zoned garnets, it can be shown that, during skarn formation, Huanggang hydrothermal fluids shifted from near-neutral pH, oxidizing conditions, and high W/R ratios with relatively low LREE/HREE ratios characteristics to acidic, reducing conditions, and low W/R ratios with relatively high LREE/HREE ratios characteristics. We infer that variations in fluid compositions and physicochemical conditions may exert major control on formation and evolution of garnets and skarn hydrothermal fluids.

**Keywords:** LA-ICP-MS trace element; zoned garnet; Huanggang skarn deposit; Southern Great Xing’an Range



**Citation:** Mei, W.; Ruan, B.; Liu, H. In Situ LA-ICP-MS of Zoned Garnets from the Huanggang Skarn Iron–Tin Polymetallic Deposit, Southeastern Mongolia, Northern China. *Minerals* **2023**, *13*, 450. <https://doi.org/10.3390/min13030450>

Academic Editors: Dimitrina Dimitrova, Kunfeng Qiu and Callum Hetherington

Received: 14 December 2022

Revised: 15 March 2023

Accepted: 19 March 2023

Published: 22 March 2023



**Copyright:** © 2023 by the authors. Licensee MDPI, Basel, Switzerland. This article is an open access article distributed under the terms and conditions of the Creative Commons Attribution (CC BY) license (<https://creativecommons.org/licenses/by/4.0/>).

## 1. Introduction

Garnet, typically the main component of skarn mineralization, is a highly refractory mineral that incorporates a broad range of trace elements at concentrations measurable by laser-ablation inductively coupled plasma mass spectrometry (LA-ICP-MS) [1–3]. Numerous studies have shown that metamorphic and magmatic garnets are able to fractionate HREE, making them very useful as geochemical tracers and in geochronological studies [4–6]. During contact metamorphism and hydrothermal alteration of carbonate-bearing rocks, garnet grows under a variety of physicochemical conditions and displays complex, oscillatory chemical zoning patterns [7–9].

In natural systems, oscillatory zoning is a frequently-described phenomenon in grossular–andradite garnets and grossular–almandine solid solutions [1,10,11] as well as in a wide range of minerals from different geological environments [12–14]. Chemical zoning of garnet has been used to solve various geological problems including understanding physicochemical conditions for the formation of minerals and rocks [15,16], identifying structural deformation, and T–P changes in orogenic belts [8,17], recording regional metamorphism history [18,19], and reflecting hydrothermal fluid evolution of skarn deposits [1,11,20–22]. The Huanggang deposit is the most important and largest skarn Fe–Sn polymetallic deposit in the Southern Great Xing’an Range of Northeast China. It was discovered in 1986 and was intensely studied. However, previous research has focused on petrogenesis and tectonic implications of the ore-forming granites [23,24], geochronology [24,25], origin of fluid [26], genesis of magnetite, and the Huanggang deposit [27,28]. Few studies have examined the microscopic features, trace element systematics, and genesis of zoning garnets within Huanggang skarn systems.

In this study, we report new textural characteristics, and systematic major, trace, and rare earth element (REE) concentrations of oscillatory zoning patterns in andradite–grossular garnets from the Huanggang Fe–Sn skarn deposit, obtained by electron microprobe and in situ laser-ablation inductively coupled plasma mass spectroscopy (LA-ICP-MS) analytical techniques. We aim to decipher origins and fluid evolution of the complex zoning patterns in garnet. Combined with fluid inclusion studies, the zoning patterns could: (1) investigate the relationship between F and Al in garnets; (2) reveal the mechanism behind incorporation of trace elements and REEs into different parts of oscillatory zoning garnets; (3) reconstruct the evolution of skarn hydrothermal fluids during garnet growth; (4) help to explain the origin of the Huanggang deposit.

## 2. Geological Background

### 2.1. Regional Setting

The Huanggang skarn iron–tin polymetallic deposit is located in the Southern Great Xing’an Range metallogenic belt, Northeast China (Figure 1a). The region recorded the evolution of the Paleo-Asian Ocean during the Paleozoic [29] and the intra-plate orogeny during the Mesozoic [30]. Both Permian and Jurassic units formed the main part of the NE-trending Huanggangliang Anticlinorium in the study area [31]. Intense NE-trending magmatic activity occurred in the area (Figure 1b). The Northeast of China experienced five stages of magmatism (240–205 Ma, 190–165 Ma, 155–145 Ma, 140–120 Ma, and 115–100 Ma) [32]. The intrusive activity of the Southern Great Xing’an Range peaked in the Late Mesozoic (ca. 155–120 Ma), simultaneous with large-scale mineralization [33]. The metallogenic belt contains three metallogenic sub-belts from west to east [34]. The Huanggang deposit occurred in the Sn-polymetallic metallogenic sub-belt, which is 20 km wide and is a large zone of concentrated tin ore in Northern China, including the Huanggang, Dajing, Bianjiadayuan, Anle, Weilasituo, Daolundaba, Aonaodaba, Haobugao, Shuangjianzishan, and Baiyinnuoer Sn-polymetallic deposits (Figure 1b).

### 2.2. Ore Deposit Geology

#### 2.2.1. Stratigraphy

The stratigraphic units, listed from south to north, consist of the lower Permian Qingfengshan Formation, Dashizhai Formation, and Huanggangliang Formation, the upper Permian Linxi Formation, and the Jurassic. The Jurassic rocks unconformably overlie the Permian strata. Both the skarn and mineralization are hosted within the lower Permian upper Dashizhai Formation and lower Huanggangliang Formation (Figure 2a). The upper Dashizhai Formation is 250–375 m thick and characterized by andesite, and the lower Huanggangliang Formation ranges from 125 to 250 m in thickness and is dominated by marble [35].

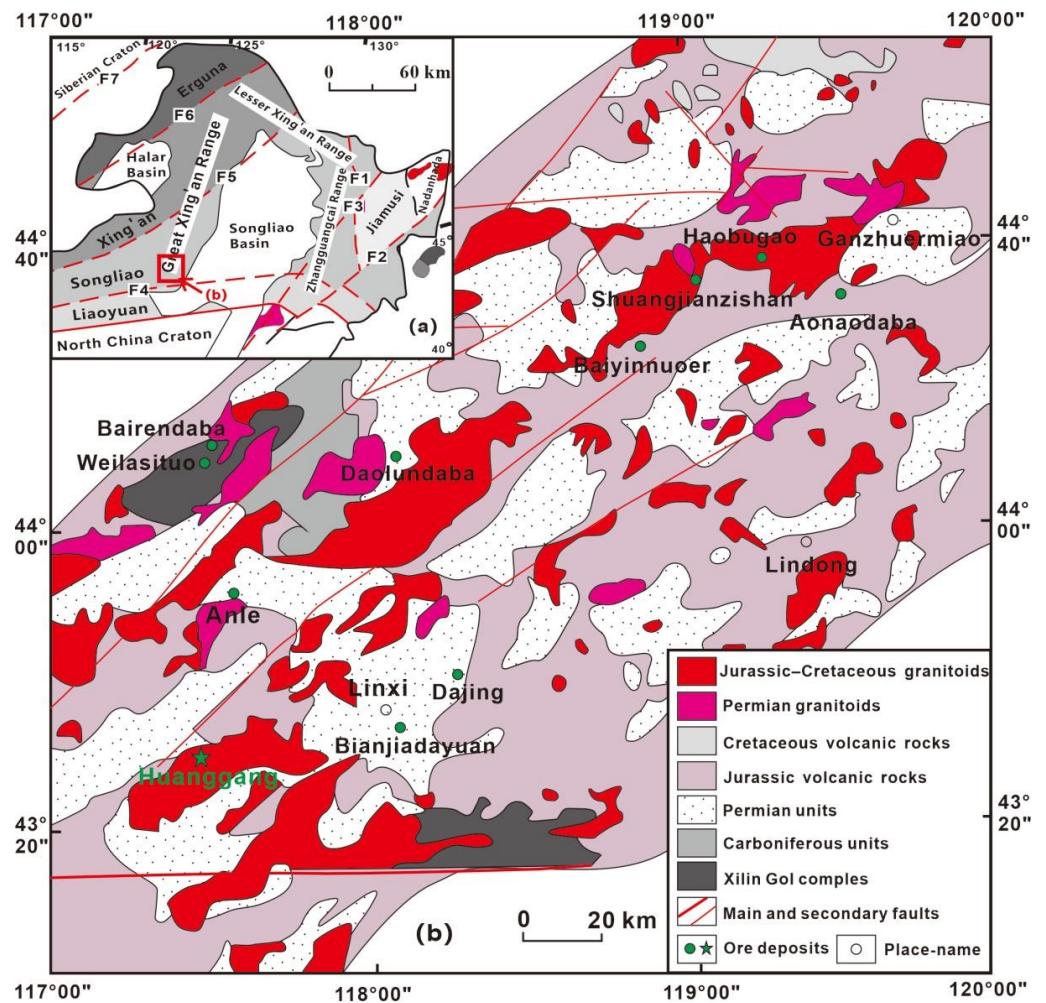


**Figure 1.** (a) Tectonic subdivisions of NE China [30]; (b) Regional geological map of the Southern Great Xing'an Range [31]. F1—Mudanjiang fault; F2—Dunhua–Mishan fault; F3—Yitong–Yilan fault; F4—Xilamulun–Changchun fault; F5—Hegenshan–Heihe fault; F6—Tanyuan–Xiguitu fault; F7—Mongol–Okhotsk fault.

### 2.2.2. Structures

The Huanggang deposit is controlled by the Huanggang–Ganzhuermiao fault [35]. The fault in the district consists of numerous fault sets with various orientations (Figure 2a): a set of NE-trending compressive shear faults (F1, F2, F3, F4, F5, and F6), a set of NW-trending tensile shear faults (F7, F8, and F9), and a set of EW-trending normal faults (F10 and F11). In general, the distributions of the mineralizations and skarn alterations are mainly controlled by the NE-trending faults (F3 and F4). Faults F3 and F4 are 8–10 km long, strike 45–50° N, dip 50–70° N, and serve as the major ore-controlling structures by providing a trap for the skarn alteration and subsequent mineralization [35].

### 2.2.3. Igneous Intrusions

Igneous intrusions are distributed along a discontinuous NE-trending zone measuring 15.4 km long by 2 km wide. These intrusions are divided into four sections based on their exposure patterns. The two largest intrusives are the Luotuochangliang intrusion and the 204 intrusion (Figure 2a), which control the ore bodies of the Western ore district (SKI, SKII, and SKVII districts) and the Eastern ore district (SKIII and SKIV districts), respectively. The intrusive rocks associated with the Huanggang deposit are the moyites, which are geochemically similar to the intra-plate A-type granitoids and yield U–Pb ages ranging

from 137 Ma to 145 Ma [23–25], which is synchronous with the mineralization age 135 Ma based on the Re-Os dating of the molybdenite from the sulfide stage [25].

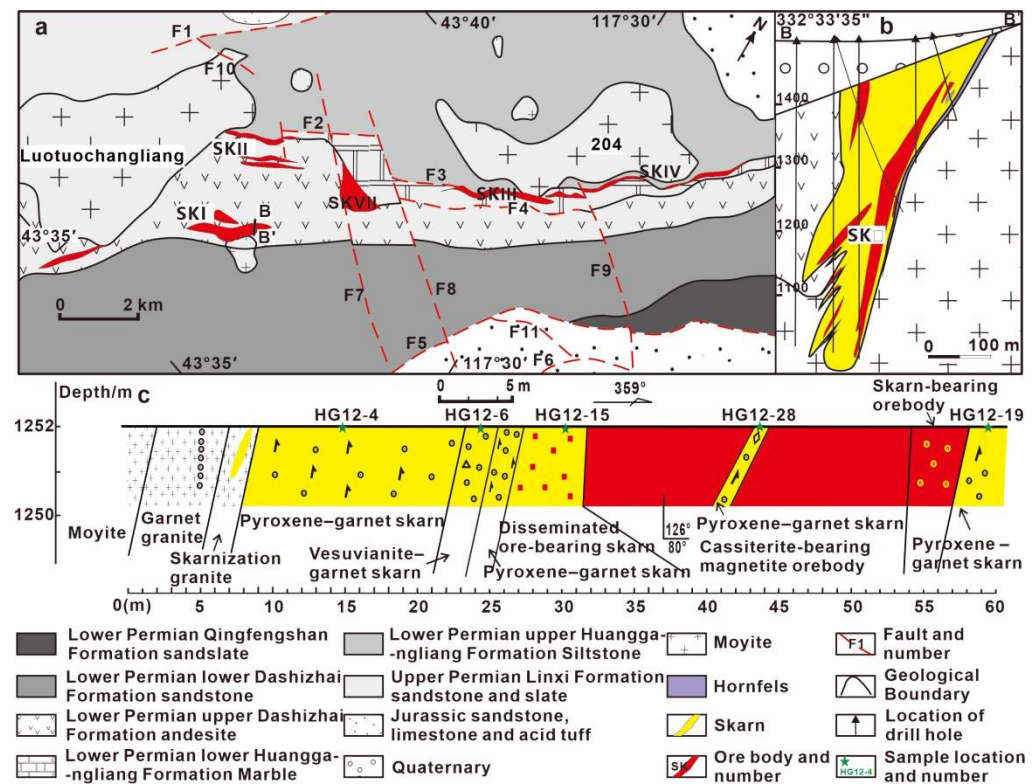


**Figure 2.** (a) Geological map of the Huanggang mining area; (b) Geological section along exploration line 70 of SKI district in Huanggang Deposit; (c) Geological horizontal section showing the zonation of skarn and mineralization at depths of 1250 m in the SKI district ((a) and (b), modified from IMGIT, 1983 [35]).

#### 2.2.4. Skarns

Many skarns are distributed in a NE-trending zone measuring 10 to 15 km in length by 0.5 to 2 km in width (Figure 2a). These skarns, which occur as lenses, are particularly important due to their spatial associations with the ore bodies, either surrounding them or scattered within them (Figures 2b and 3d). The garnet skarns (more garnets than pyroxene) are predominant in this deposit. Samples of garnet-bearing skarn were collected from a horizontal section at depths of 1250 m in the SKI district, and display the representative skarn sequence: moyite → garnet granite → pyroxene–garnet skarn → vesuvianite–garnet skarn → disseminated ore-bearing skarn → cassiterite-bearing magnetite ore body cut by pyroxene–garnet skarn vein → skarn-bearing ore body → pyroxene–garnet skarn (Figure 2c).

The skarn mineral assemblages consist of garnet (80%), pyroxene (10%), wollastonite (5%), amphibole (3%), and chlorite (2%), which is typical of a calcareous skarn. Electron microprobe analyses indicate that the garnet and pyroxene compositions are mainly andradite, grossular, diopside, and hedenbergite [28]. Replacements of garnet, pyroxene, and vesuvianite by chlorite, quartz, calcite, and fluorite are common (Figure 5c,f). It is worth mentioning that Mn-bearing skarn minerals (such as spessartine and johannsenite) are widely distributed in the Huanggang deposit and other skarn deposits (Baiyinuoe, Haobugao) from the Southern Great Xing’an Range [34].

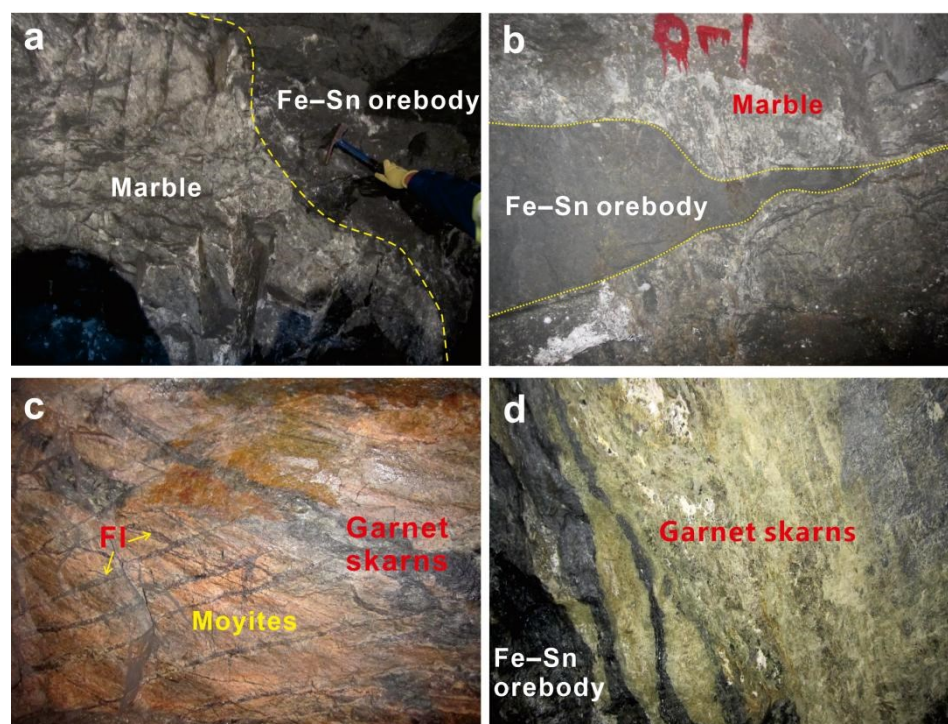


**Figure 3.** Relations between ore body, alteration, and host rocks. (a) Most of the Fe–Sn ore bodies are irregularly lamellar or lenticular and located within the contact zone between marble and moyites; (b) Some of the Fe–Sn ore bodies are veined interspersed marble; (c) Fluorite mainly replaced the garnet skarns and moyites as a banding distribution; (d) Garnet skarns occur either surrounding them or scattered within them as lenses.

### 2.2.5. Mineralization and Alteration

The Huanggang deposit is the largest iron–tin polymetallic deposit in the Southern Great Xing’an Range, with a proven reserve of 10,829 Mt Fe at an average grade of 33–45 wt.% Fe [35]. Most of the ore bodies are irregularly lamellar or lenticular and located within the contact zone, but some of them are veined interspersed marble (Figure 3a,b). The ore body exposures in the Huanggang deposit are 19 km long and 0.2 to 2.5 km wide. The ore body strikes NE 48–62°, dips 40–80° N, and is exposed at elevation between 955 and 1775 m above sea level (Figure 2b). The thicknesses of the ore bodies vary from 2 to 118 m (average 25 m). The ore minerals are predominantly magnetite with minor cassiterite, scheelite, molybdenite, sphalerite, chalcopyrite, galena, arsenopyrite, pyrite, hematite, tetrahedrite, and stannite. The host rock alteration consists of skarnification, fluoritization, carbonatization, and silicification (Figure 3c) [26].

The paragenetic sequence of the Huanggang deposit can be divided into three stages of hydrothermal activity according to a previous study [26]: a prograde skarn stage (I), a retrograde skarn stage (II), and a sulfide stage (III). Existing isotope studies (H–O, S, Pb) suggest that the Huanggang skarn iron–tin polymetallic deposit was formed from a magmatic–hydrothermal system. Fluid inclusion data of three hydrothermal stages demonstrated that the ore-forming fluids displayed decreasing temperature and decreasing salinity characteristics. Both fluid boiling and mixing may have played an important role for the Huanggang skarn mineralization [26].

### 3. Analytical Methods

All samples were prepared as polished thin sections and subsequently examined using optical microscopy to observe the mineralogical and textural relationships, with an emphasis on the occurrence, morphology, and texture of garnet. The polished thin sections

were used for back-scattered electron (BSE), electron probe microanalysis (EPMA), and laser-ablation inductively coupled plasma mass spectrometer (LA-ICP-MS) analysis.

### 3.1. Back-Scattered Electron (BSE) and Electron Probe Micro-Analysis (EPMA)

Back-scattered electron (BSE) images of garnets were acquired by an FEI Quanta 200 environmental scanning electron microscope (Hillsboro, OR, USA) equipped with an energy-dispersive spectrometer at the State Key Laboratory of Geological Process and Mineral Resources of the China University of Geosciences, Wuhan. Unknown minerals were semi-quantitatively analyzed by energy-dispersive X-ray spectrometry with 1  $\mu\text{m}$  beam diameter at an accelerating voltage of 20 kV at the same laboratory. EPMA analysis of garnet was conducted using a JXA-8230 Superprobe at the Center for Material Research and Analysis, Wuhan University of Technology (WUT). Standards and unknowns were analyzed with 1  $\mu\text{m}$  beam diameter at an accelerating voltage of 20 kV and a beam current of 20 nA. Integration time for peaks of Al, Si, and Mg are 30 s, and for the remaining elements are 20 s. The following standards were used: jadeite (Si and Al), forsterite (Mg), wollastonite (Ca), rutile (Ti), and synthetic oxide (Cr, Mn, Fe, and Ni), vanadium (V), Fluorite (F), and cassiterite (Sn).

### 3.2. Laser-Ablation Inductively Coupled Plasma Mass Spectrometry (LA-ICP-MS)

Trace elements and REEs were analyzed by LA-ICP-MS at Nanjing FocuMS Contract Testing Co. Ltd. (Nanjing, China). The Teledyne Cetac Technologies Analyte Excite laser-ablation (LA) system (Bozeman, MT, USA) and the Agilent Technologies 7700x inductively coupled plasma mass spectrometer (ICP-MS) (Hachioji, Tokyo, Japan) were combined for the experiments. The 193 nm ArF excimer laser, homogenized by a set of beam delivery systems, was focused on garnet surfaces with a fluence of 6.0 J/cm<sup>2</sup>. Ablation protocol employed a spot diameter of 35  $\mu\text{m}$  at a 7 Hz repetition rate for 40 seconds (equating to 280 pulses). Helium was applied as the carrier gas to efficiently transport aerosols to the ICP-MS. Multiple external reference materials (GSE-1G, BCR-2G, BIR-1G and BHVO-2G) were used to calibrate element contents [36]. GSE-1G was used as a quality control to correct the time-dependent signal drift and mass discrimination. Raw data reduction was performed off-line by ICPMSDataCal software using a 100%-normalization strategy [36].

## 4. Results

### 4.1. Garnet Petrography

According to spatial relationships among alteration mineral assemblages, the sampled garnet grains were mainly formed during mineralization stages I and II (Table 1). Samples HG12-4 and HG12-6 are representative of the prograde skarn stage, and sample HG12-4 was collected from the location near the moyite, but sample HG12-6 was close to the ore body. Sample HG12-15, at an early retrograde skarn stage, was collected from the ore body. Both samples of HG12-19 and HG12-28 represent the late retrograde skarn stage. The former was in sharp contact with the ore body (Figure 2c), and the latter cut across the ore body as veins (Figures 2c and 4e). The detailed ore textures, mineral assemblages, and occurrences of garnet are described as following.

**Table 1.** Sampling of garnets from various mineralization stages in the Huanggang deposit.

Sample Number	Sample Name	Mineralization Stage	Sampling Site
HG12-4	the pyroxene–garnet skarn	the early prograde skarn stage	collected near the moyite at depths of 1250 m in the SKI district
HG12-6	the vesuvianite–garnet skarn	the late prograde skarn stage	collected in close proximity to the ore body at depths of 1250 m in the SKI district

Table 1. Cont.

Sample Number	Sample Name	Mineralization Stage	Sampling Site
HG12-15	the disseminated ore-bearing skarn	the early retrograde skarn stage	collected from the disseminated ore body at depths of 1250 m in the SKI district
HG12-19	the giant-grained black garnet skarn	the late retrograde skarn stage	collected from the sharp contact with the ore body at depths of 1250 m in the SKI district
HG12-28	the pyroxene–garnet skarn	the late retrograde skarn stage	across the Sn-Fe ore body as veins at depths of 1250 m in the SKI district

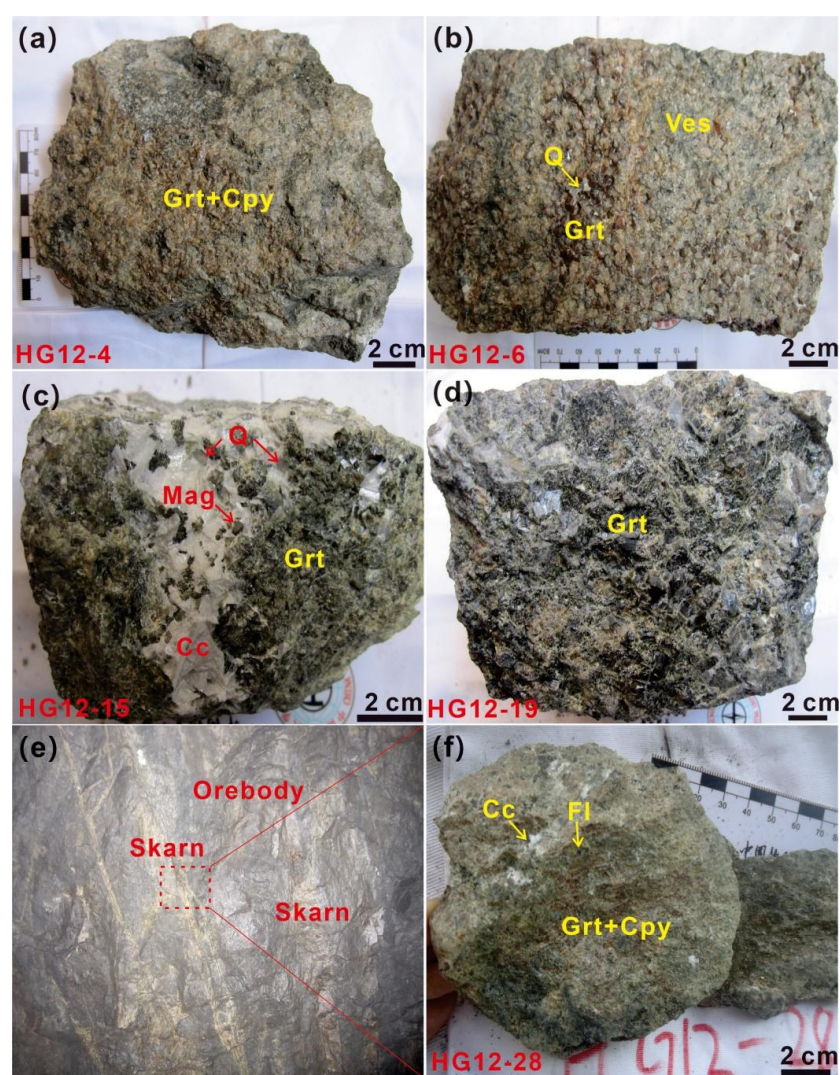


**Figure 4.** The field observation and microscope photographs of garnet skarn from different mineralization stages of the Huanggang deposit. (a) Massive pyroxene–garnet skarn (sample HG12-4). (b) Massive vesuvianite–garnet skarn surrounded by the quartz (sample HG12-6). (c) Disseminated ore-bearing skarn cut by later quartz and calcite veins (sample HG12-15). (d) Massive giant-grained black garnet skarn (sample HG12-19). (e) The later skarn (sample HG12-28) cut across the massive ore body as veins. (f) Clinopyroxene–garnet skarn surrounded by fluorite and calcite. Mineral abbreviations: Grt, garnet; Cpy, clinopyroxene; Ves, vesuvianite; Q: quartz; Cc, calcite; Mag, magnetite; Fl: fluorite.

The early prograde skarn stage is defined by massive skarn (sample HG12-4) consisting of brown fine-grained garnet and clinopyroxene (Figure 4a). Two distinct garnet generations could be identified based on their optical and textural characteristics. In detail, the first garnet generation (Grt I) is generally yellow and isotropic with subhedral crystal. The second garnet generation (Grt II) is generally colorless, and anisotropic with oscillatory zoning. In this stage, garnet is characterized by the isotropic core (Grt I) but with an oscillatory zoned rim (Grt II) which is cut by later fractures (Figures 5a,b and 6a), Electron microprobe analyses indicate that the garnet is intergrown with the hedenbergite (Figure 5a,b).

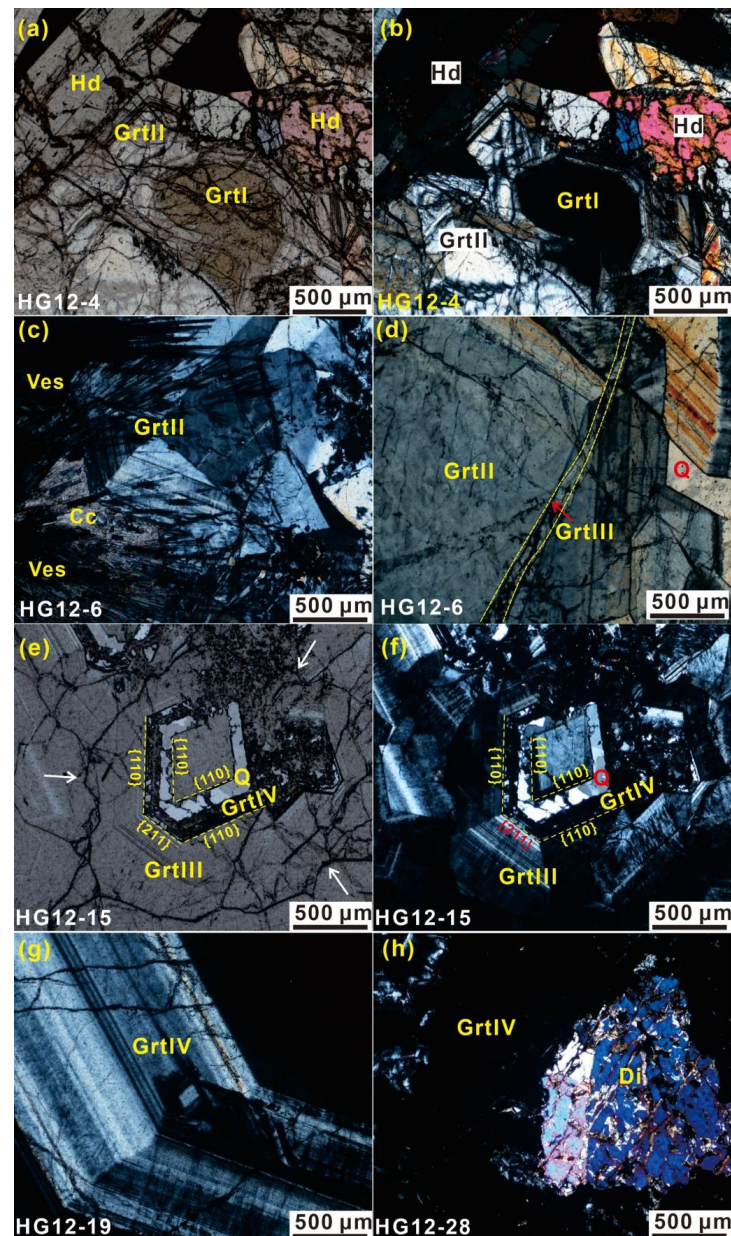


**Figure 5.** Transmitted light photomicrographs under crossed polarized light-XPL (a,d,e) and plane polarized light-PPL (b,c,f,g,h) showing optical and textural characteristics of garnets from the Huanggang deposit. (a,b) The garnets from the sample HG12-4 with the yellow core (Grt I) and colorless zoned rim (Grt II). (c,d) The Grt II from sample HG12-6 cut across by the later anisotropic garnet vein (Grt III). (e,f) Grt III replaced by later quartz and residual garnet (Grt IV). (g) Grt IV of sample HG12-19 showing obvious core–rim texture. (h) Grt IV of sample HG12-28 intergrown with diopside. Mineral abbreviations: Grt, garnet; Hd, hedenbergite; Ves, vesuvianite; Cc, calcite; Q, quartz; Di, diopside.

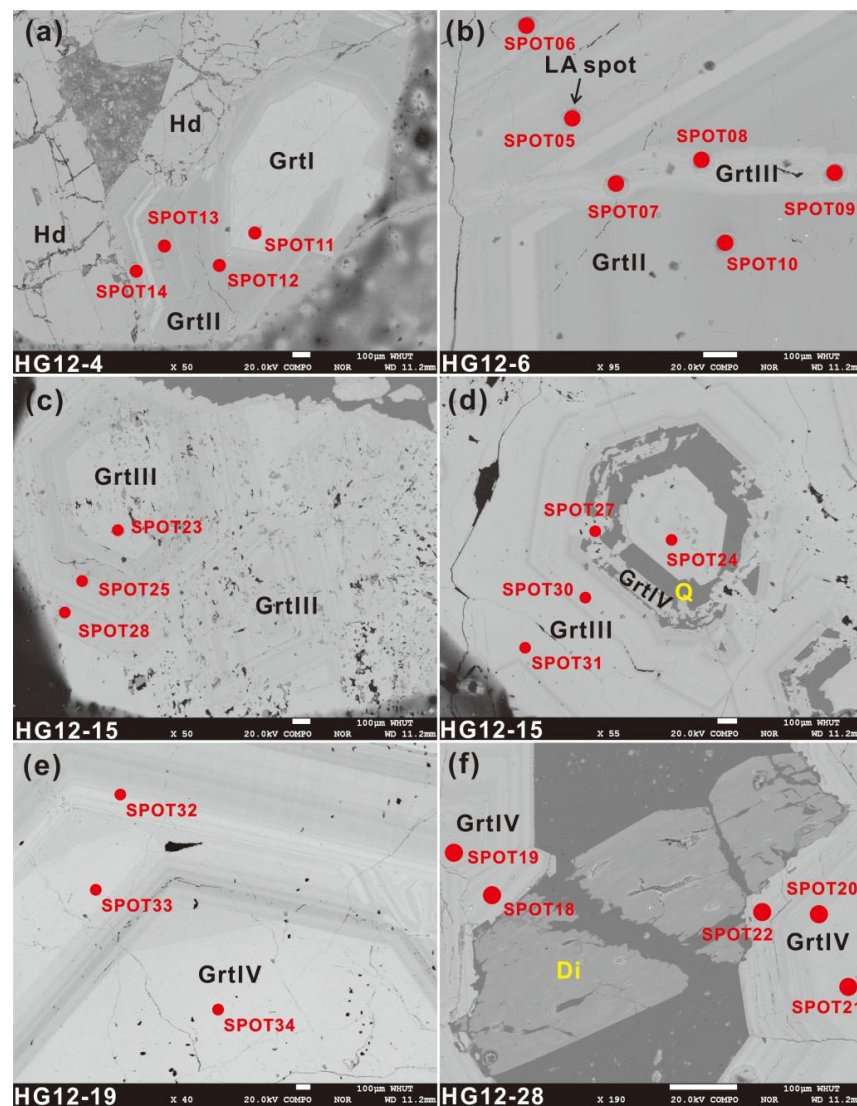


**Figure 6.** Back-scattered electron (BSE) images of the garnets from the Huanggang deposit. (a) The garnet (sample HG12-4) showing the isotropic core (Grt I) and oscillatory zoned rim (Grt II). (b) The garnet (sample HG12-6) exhibiting the oscillatory zoning of garnet (Grt II) cut by garnet veins (Grt III). (c,d) The garnet (Grt III) displaying the obvious core–rim texture, whose alteration of garnet is serious, and also replaced by later irregular residual garnet (Grt IV). (e,f) The garnet (Grt IV) exhibiting obvious core–rim texture, and also intergrown with diopside. Mineral abbreviations: Grt, garnet; Hd, hedenbergite; Q, quartz; Di, diopside.

The late prograde skarn stage is characterized by massive skarn composed of brown coarse-grained garnet and vesuvianite skarn (sample HG12-6) (Figure 4b). These euhedral garnet crystals (Grt II) exhibit obvious twinning and zoned texture, intergrown with radial vesuvianite, and later, calcite and quartz fill the interstitial spaces of the garnets (Figure 4c,d). The third garnet generation (Grt III) is anisotropic and overprints pre-existing garnet (Grt II) as veins (Figure 5d). Back-scattered electron (BSE) imaging shows that the oscillatory zoning of garnet (Grt II) is displaced and cut by garnet veinlets (Grt III) (Figure 6b).

The early retrograde skarn stage is greyish-green garnet skarn (sample HG12-15) containing some disseminated magnetite grains, and cut by later quartz and calcite veins (Figure 4c). In general, the anisotropic third garnet generation (Grt III) displays obvious core–rim textural features: the core shows simple dodecahedral {110} growth without zoned features, the rim shows a composite dodecahedral {110}-trapezohedron {211} growth with obvious twinning and oscillatory zoning (Figure 5e,f). Back-scattered electron (BSE)

imaging shows that the alteration of garnet (Grt III) is serious (Figure 6c), noting that the later garnet (Grt IV) is irregular and isotropic, which replaced the earlier garnet (Grt III) along the pore between the core and rim with the quartz (Figures 5e,f and 6d). Additionally, the presence of many fractures in garnet crystals can be observed (Figures 5e and 6d).

The late retrograde skarn stage resulted in garnet skarns including sample HG12-19 and sample HG12-28. Sample HG12-19 is made of giant-grained black garnet (Figure 4d), sample HG12-28 cut across the earlier iron–tin ore body as veins (Figure 4e), consisting of red garnet and clinopyroxene surrounded by fluorite and calcite (Figure 4f). Two samples of fourth garnet generations (Grt IV) exhibit obvious core–rim texture: the core is isotropic, and the rim is anisotropic with various zoning (Figures 5g,h and 6e,f). In contrast, sample HG12-28 is smaller in size, and intergrown with diopside (Figures 5h and 6f).

#### 4.2. Major Element Compositions of Garnet

The EPMA results for the garnets from the Huanggang deposit are presented in Table S1, and show that garnets form grossular–andradite solid solution compositions that range from  $\text{And}_{22.48}\text{Gro}_{72.47}$  to almost pure andradite  $\text{And}_{97.60}\text{Gro}_{0.88}$  with pyralspite less than 10% (Figure 7a). Changes in the major element compositions of these garnets correlate with the different garnet petrographic characteristics described in the previous section. The garnets from the prograde skarn stage contain significant amounts of Al, whereas those from the retrograde skarn stage are relatively rich in Fe (Figure 7b). This is consistent with the majority of skarn systems that are characterized by early formed Al-enriched and later-formed Fe-enriched garnets [37–39].

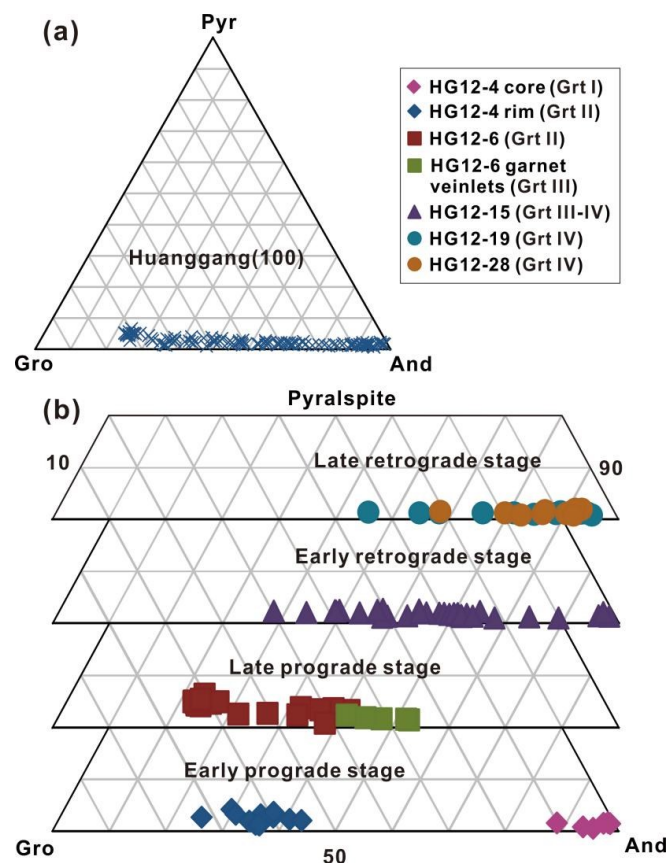


**Figure 7.** Major element compositions of the garnets from the Huanggang deposit. (a) Ternary diagram summarizing approximately 100 data of the garnets. (b) Ternary diagram summarizing the compositional variations in garnets from the prograde skarn stage to the retrograde skarn stage. Abbreviations: Gro, grossular; And, andradite; Pyr, pyralspite = pyrope + spessartine + almandine + uvarovite.

Based on the morphological and compositional variation, four typical types of garnet (Grt I to Grt IV) may be identified in the Huanggang deposit.

The garnet (HG12-4) from the early prograde skarn stage is characterized by the earlier isotropic andradite (Grt I) in the core but with an oscillatory zoning grossular (Grt II) in the rim. In the grossular (Grt II), the Al content decreases from the inner to the external, whereas the  $\text{Fe}^{3+}$  content increases (Figure 8a). The MnO abundance decreases from the inner to the external in the grossular (GrtII), whereas it is stable in the andradite (Grt I) (Figure 9a). The garnets (HG12-4) from the Huanggang deposit are F-enriched, with the first- and second-generation garnets containing 0.00–0.88 (average 0.24) wt.% F (Figure 10a).

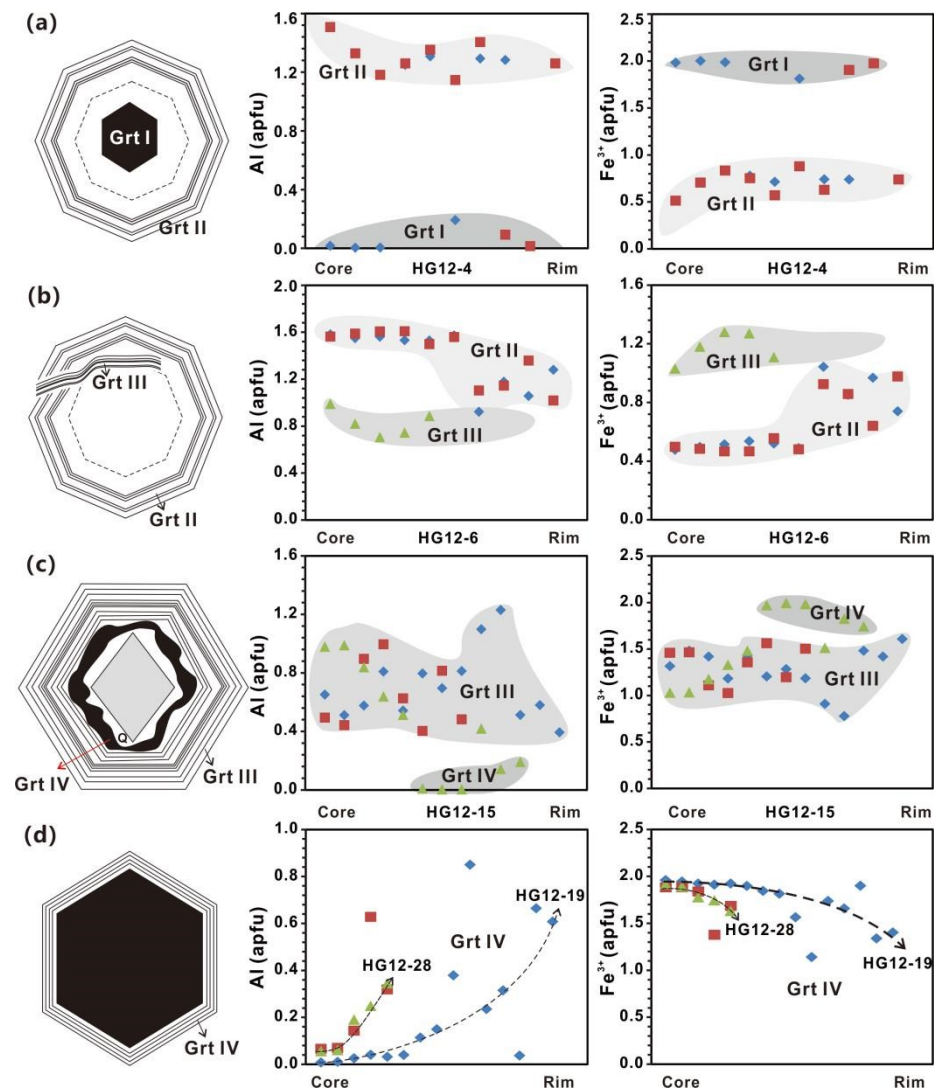


**Figure 8.** Four typical types of garnet morphology in the Huanggang deposit, and associated compositional variations.

The garnet (HG12-6) from the late prograde skarn stage is mainly composed of the anisotropic grossular (Grt II) cut by irregular fine-veined  $\text{Fe}^{3+}$ -rich andradite (Grt III). The Al content sharply decreases from the core to the rim of the grossular (Grt II), whereas the  $\text{Fe}^{3+}$  content abruptly increases (Figure 8b). MnO abundance obviously decreases from the core to the rim of the grossular (Grt II), even to the later  $\text{Fe}^{3+}$ -rich andradite veinlet (Grt III) (Figure 9b). The garnets (HG12-6) yield much more F content, ranging from 0.00% to 1.43% (average 0.43%) (Figure 10a).

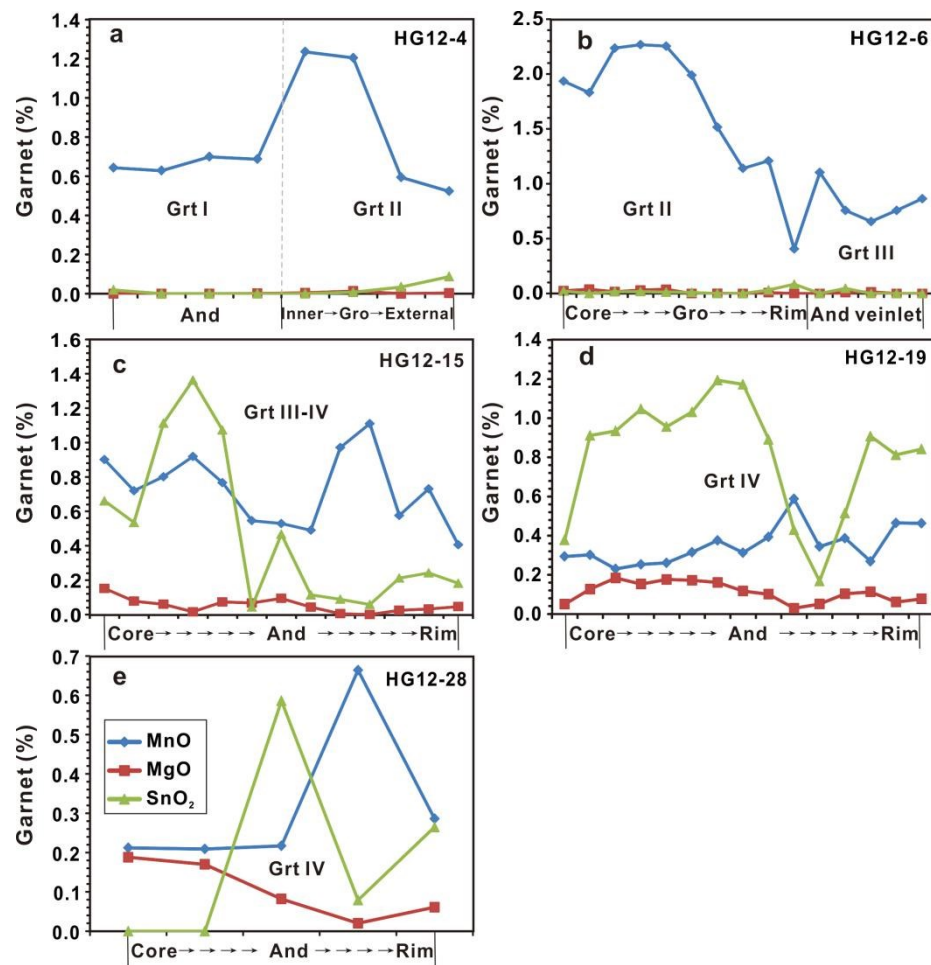


Figure 9. MnO, MgO, and SnO<sub>2</sub> content variations in the garnets of different mineralization stages from the Huanggang deposit.

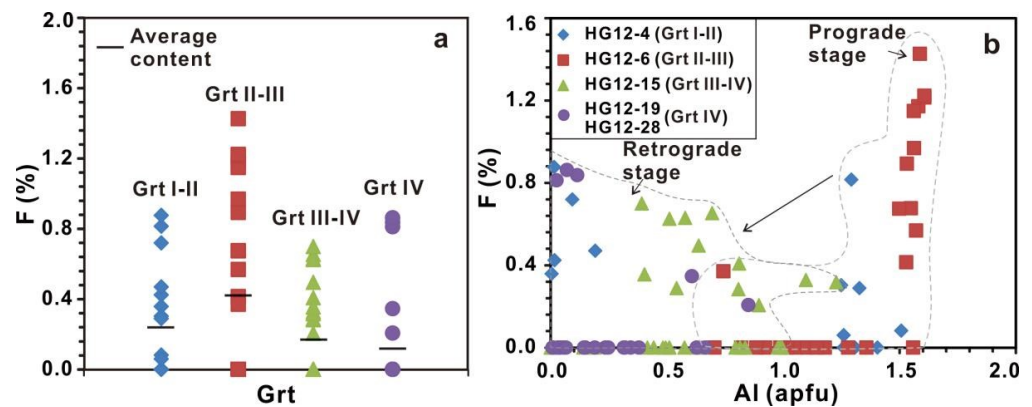


Figure 10. (a) F concentrations in garnets from the Huanggang deposit. (b) F concentrations versus total Al in atoms per formula unit (apfu) from the Huanggang deposit.

The garnet (HG12-15) from the early retrograde skarn stage is defined by Fe<sup>3+</sup>-rich, Al-poor anisotropic andradite (Grt III) and some later isotropic andradite (Grt IV) which is characterized by the metasomatic relict texture located between the core and rim of the Grt III. The Fe<sup>3+</sup> and Al contents are varied from the core to the rim of the Fe<sup>3+</sup>-rich andradite (Grt III) (Figure 8c), whereas the MnO and SnO<sub>2</sub> abundances decrease. The MgO content of the Fe<sup>3+</sup>-rich andradite (Grt III) from the retrograde skarn stage is stable (Figure 9c).

The garnets (HG12-15) contain much lower F concentrations, ranging from 0.00% to 0.70% (average 0.17%) (Figure 10a).

The garnet (HG12-19, HG12-28) from the late retrograde skarn stage is featured by the andradite (Grt IV) with an isotropic core and oscillatory zoned rim. The Al content increases gradually, whereas the  $\text{Fe}^{3+}$  content decreases from the core to the rim of the andradite (Grt IV) (Figure 8d). The MnO and  $\text{SnO}_2$  abundances increase from the core to the rim, but the MgO abundance is decreased (Figure 9d). The F contents of the andradite (Grt IV) are in the range of 0.00% to 0.86% (average 0.12%) (Figure 10a).

The results of BSE and EPMA show that garnets have various morphological, textural, and compositional characteristics in different mineralization stages: (1) The prograde skarn stage is defined by a grossular (Grt II) with minor andradite core (Grt I) or cut by  $\text{Fe}^{3+}$ -rich andradite (Grt III) veinlets. The Al content gradually decreases from the core to the rim, whereas the  $\text{Fe}^{3+}$  content increases. These garnets have lower Mg (0.00–0.06%) and  $\text{SnO}_2$  (0.00–0.09%), higher Mn (0.21–2.90%) and F (0.00–1.43%) contents; (2) The retrograde skarn stage is characterized by  $\text{Fe}^{3+}$ -rich andradite (Grt III) and andradite (Grt IV). The  $\text{Fe}^{3+}$  content gradually decreases from the core to the rim, whereas the Al content increases. These garnets have higher Mg (0.00–0.24%) and  $\text{SnO}_2$  (0.00–1.36%), and lower Mn (0.21–1.14%) and F (0.00–0.86%) abundances. In addition, a weak positive correlation is present between F and  $\text{Al}^{3+}$  at concentrations from the prograde skarn stage to the retrograde skarn stage (Figure 10b).

#### 4.3. Trace and Rare Earth Element Compositions of Garnet

Trace elements and REEs were analyzed to identify their concentrations in different part of the garnets. The results are presented in Table S2.

##### 4.3.1. Trace Elements

The garnet is depleted in large ion lithophile elements (LILE) with lower values of K, Ba, Sr, and Ti. In contrast, U, Nd, and Sm are enriched in garnets (Figure 11). This is due to the larger ionic size of these elements when compared with the size of the octahedral and eight coordination sites of the garnet structure [1,3].

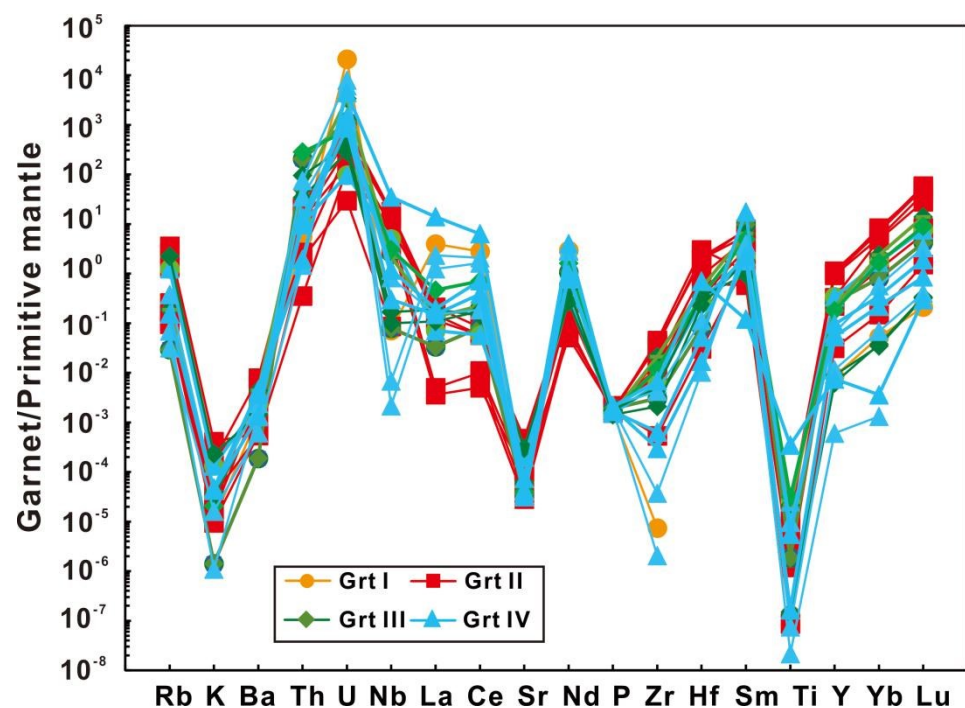
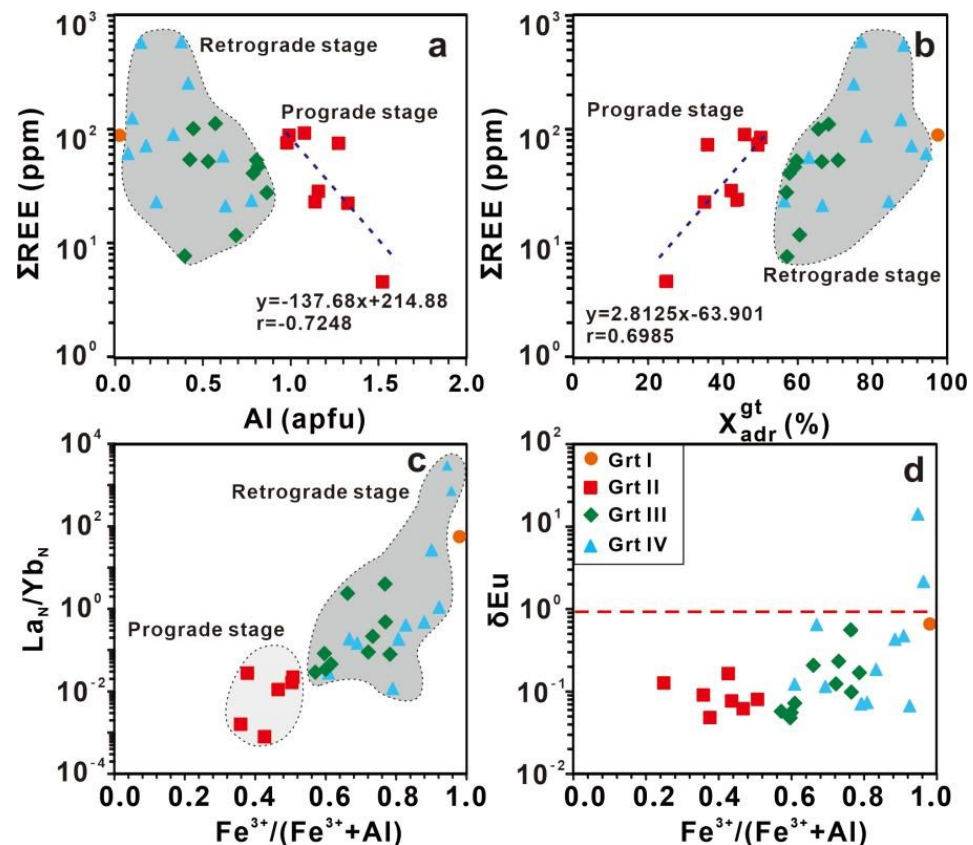


Figure 11. Trace element spider diagram of the garnets from the Huanggang deposit. Samples were normalized to the primitive mantle values of Sun and McDonough, 1989 [40].

The LA-ICP-MS data show that garnets from retrograde skarn stage are more enriched with REE than those of prograde skarn stage. There is a strong negative correlation between Al and  $\Sigma\text{REE}$  and a strong positive correlation between  $X_{\text{adr}}^{\text{gt}}$  and  $\Sigma\text{REE}$  in the prograde skarn stage (Figure 12a,b). In addition,  $\text{La}_N/\text{Yb}_N$  values show a more consistent variation with  $\text{Fe}^{3+}/(\text{Fe}^{3+} + \text{Al})$ . Garnets from the retrograde skarn stage have higher  $\text{La}_N/\text{Yb}_N$ , which indicates that the LREE/HREE fractionation increases with increasing Fe concentrations (Figure 12c). Although  $\delta\text{Eu}$  and  $\text{Fe}^{3+}/(\text{Fe}^{3+} + \text{Al})$  do not correlate, most garnets from various skarn stages have obvious negative Eu anomalies (Figure 12d). Furthermore, variations in  $\Sigma\text{REE}$ , U, and Y contents of garnets suggest that the prograde skarn stage garnets typically have relatively low U, whereas the retrograde skarn stage garnets have high U concentrations. Our data display linear relationships between U, Y, and  $\Sigma\text{REE}$  concentrations in garnets of the prograde skarn stage (Figure 13a,b). It is noticeable that there is a strong positive correlation between the andradite content,  $\delta\text{Eu}$ , and the contents of metal elements in the garnet such as W and Mo (Figure 14a–d). Although the garnets (GrtIII and GrtIV) contain the highest amounts of Sn (186.30–6357.70 ppm), the data did not display obvious linear relationships between Sn and andradite content (Figure 14e,f).



**Figure 12.** (a) Total REE concentrations ( $\Sigma\text{REE}$ ) versus total Al in atoms per formula unit (apfu) for garnets from the Huanggang deposit. (b)  $\Sigma\text{REE}$  versus percentage of the andradite (adr) end-member component in garnets. (c) LREE/HREE fractionation versus  $\text{Fe}^{3+}/(\text{Fe}^{3+} + \text{Al})$  ratio of garnets. (d) Eu anomaly ( $\delta\text{Eu}$ ) versus  $\text{Fe}^{3+}/(\text{Fe}^{3+} + \text{Al})$  ratio of garnets.

#### 4.3.2. Rare Earth Elements

The garnets of the Huanggang deposit are characterized by distinct REE patterns from Grt I to Grt IV in four typical skarn stages (Figure 15).

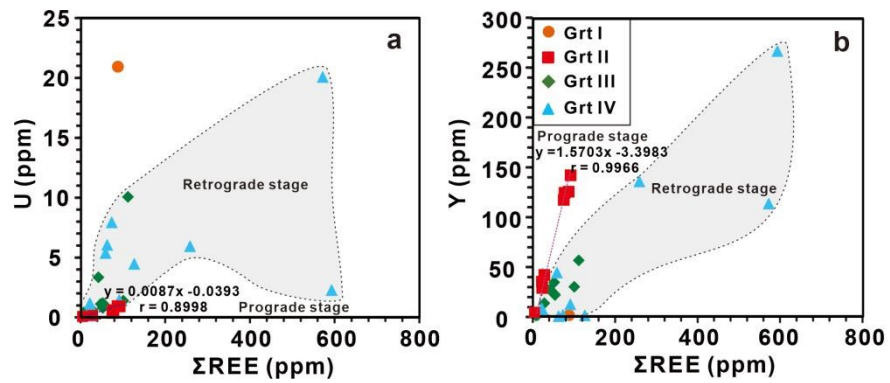


Figure 13. Variations in  $\Sigma$ REE with U (a) and Y (b) in the garnets of the Huanggang deposit.

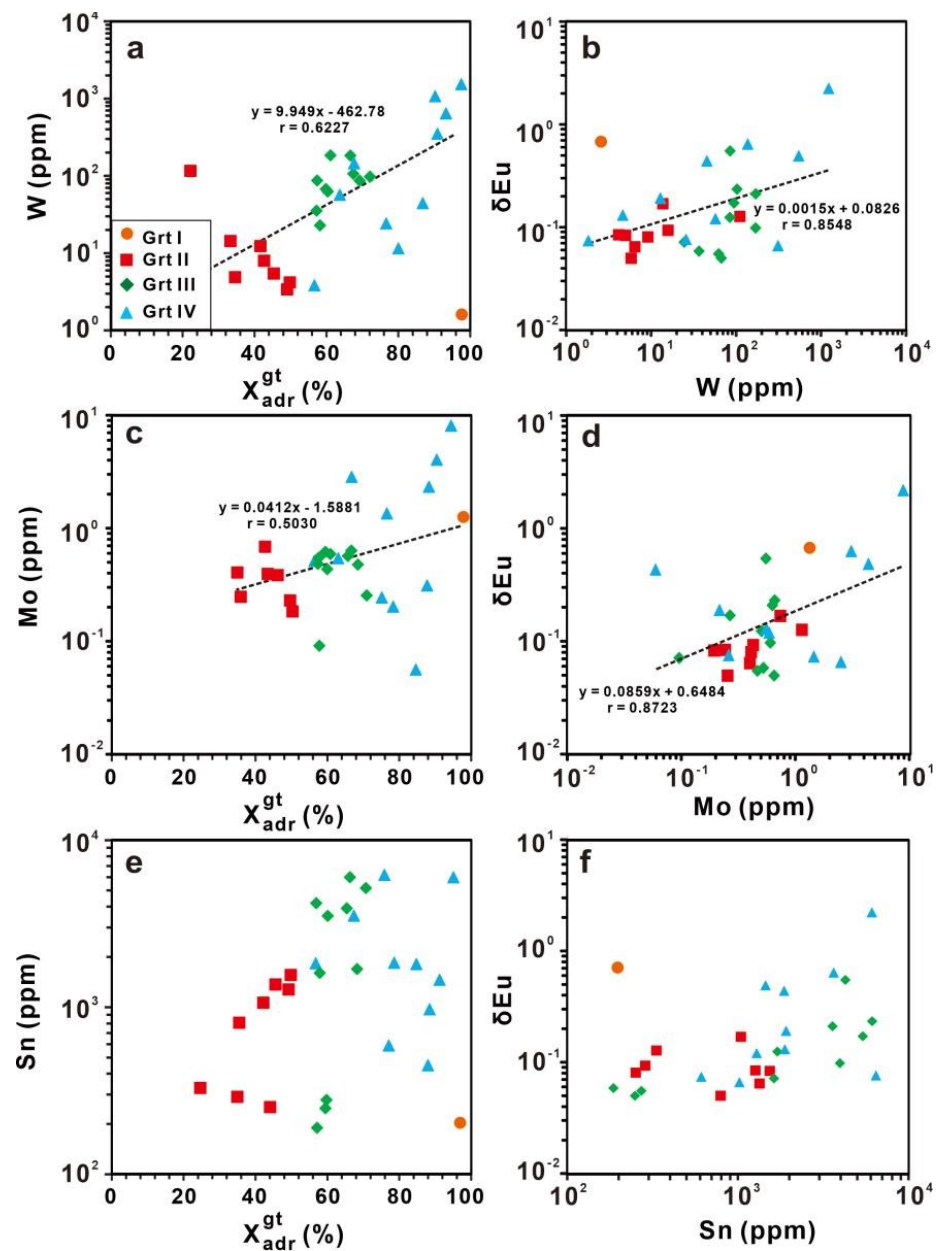
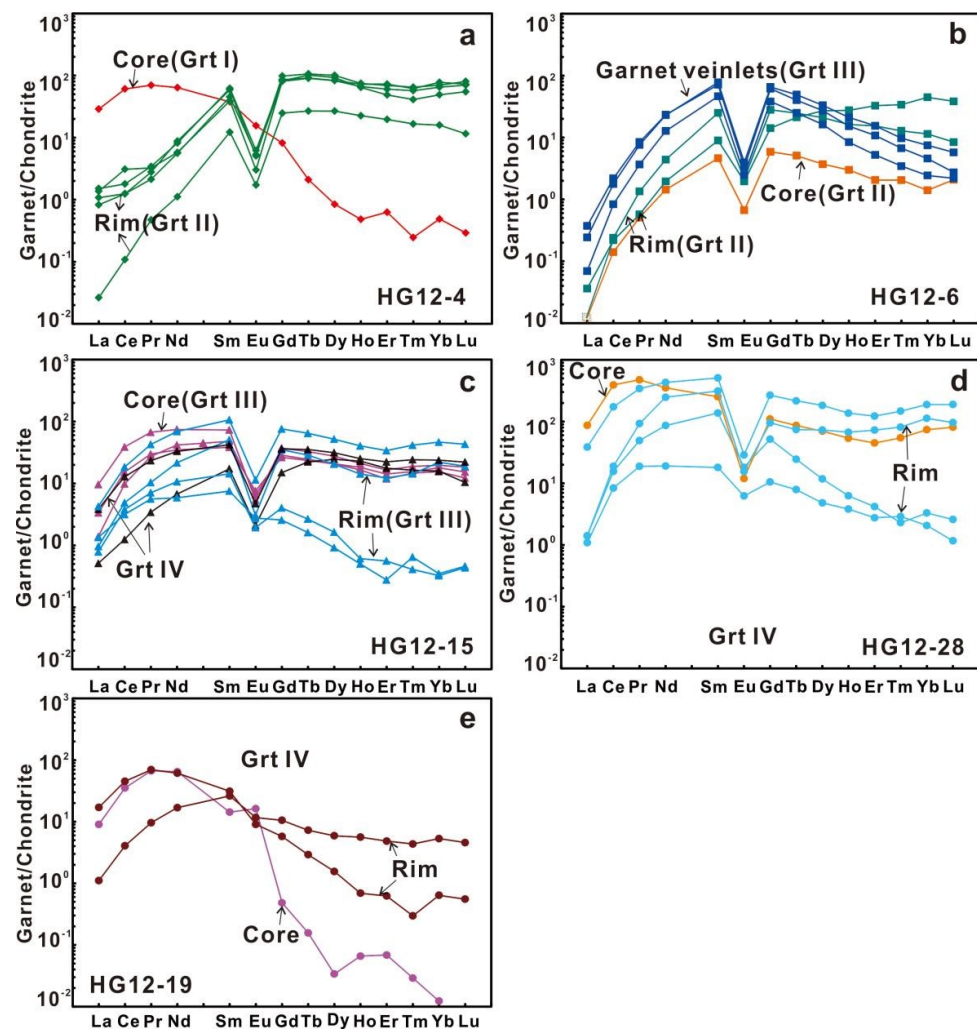


Figure 14. Diagrams of W vs.  $X_{adr}^{gt}$  (a),  $\delta Eu$  vs. W (b), Mo vs.  $X_{adr}^{gt}$  (c),  $\delta Eu$  vs. Mo (d), Sn vs.  $X_{adr}^{gt}$  (e), and  $\delta Eu$  vs. Sn (f) in garnets from different stages of Huanggang deposits.



**Figure 15.** Chondrite-normalized REE patterns of the garnets from the Huanggang deposit. Samples were normalized to the C1 values of McDonough and Sun, 1995 [41].

In the early prograde skarn stage (garnet sample HG12-4), the andradite cores (Grt I) have moderately downward-sloping trend ( $\Sigma\text{REE} = 88.29$  ppm, LREE-enriched, HREE-depleted and  $\Sigma\text{LREE}/\Sigma\text{HREE} = 40.46$ ), with weak negative Eu anomalies ( $\delta\text{Eu} = 0.68$ ). In contrast, grossular rims (Grt II) show upward-sloping-to-flat REE pattern ( $\Sigma\text{REE} = 22.61\text{--}92.26$  ppm, obviously HREE-enriched and LREE-depleted,  $\Sigma\text{LREE}/\Sigma\text{HREE} = 0.13\text{--}0.21$ ), with stronger negative Eu anomalies ( $\delta\text{Eu} = 0.05\text{--}0.09$ ) (Figure 15a).

In the late prograde skarn stage (garnet sample HG12-6), the grossulars (Grt II) have a moderately upward-sloping trend (LREE-depleted and HREE-enriched,  $\Sigma\text{LREE}/\Sigma\text{HREE} = 0.10\text{--}0.49$ ), with strong negative Eu anomalies ( $\delta\text{Eu} = 0.08\text{--}0.17$ ). The  $\text{Fe}^{3+}$ -rich andradite veinlets (Grt III) which cut the earlier grossular (Grt II) contain similar REE patterns as the grossular (Grt II), but the  $\Sigma\text{LREE}/\Sigma\text{HREE}$  ratios are larger (0.86–0.99), close to 1, and the  $\Sigma\text{REEs}$  increase from the Grt II core (4.59 ppm) through the Grt II rim (28.47 ppm) to the Grt III (28.00–52.23 ppm) (Figure 15b).

In the early retrograde skarn stage (garnet sample HG12-15), REE patterns of the  $\text{Fe}^{3+}$ -rich andradite (Grt III) have a flat trend with obvious negative Eu anomalies (Figure 15c). REE patterns of  $\text{Fe}^{3+}$ -rich andradite (Grt III) show distinct differences from the Grt III core through Grt IV to Grt III rim: (1) The Grt III cores have slightly flat REE patterns ( $\Sigma\text{REE} = 52.16\text{--}100.89$  ppm,  $\Sigma\text{LREE}/\Sigma\text{HREE} = 1.90\text{--}3.33$ ) and obviously negative Eu anomalies ( $\delta\text{Eu} = 0.10\text{--}0.23$ ); (2) The later irregular andradite (Grt IV) shows slightly upward-sloping-to-flat REE patterns ( $\Sigma\text{REE} = 24.08\text{--}58.71$  ppm, HREE-enriched, LREE-depleted, and  $\Sigma\text{LREE}/\Sigma\text{HREE} = 0.41$ ), with obviously negative Eu anomalies ( $\delta\text{Eu} = 0.12\text{--}0.13$ ); (3) The Grt

III rims have two distinct REE patterns. One rim (Figure 6d) contains similar REE patterns ( $\Sigma\text{REE} = 7.69\text{--}111.78$  ppm) to the Grt III cores, with an obviously flat trend ( $\Sigma\text{LREE}/\Sigma\text{HREE} = 1.08\text{--}1.35$ ) and obviously negative Eu anomalies ( $\delta\text{Eu} = 0.07\text{--}0.12$ ). Nevertheless, the other rims (Figure 6c) have a slightly downward-sloping trend (LREE-enriched, HREE-depleted, and  $\Sigma\text{LREE}/\Sigma\text{HREE} = 6.86\text{--}7.08$ ), with moderately negative Eu anomalies ( $\delta\text{Eu} = 0.21\text{--}0.55$ ).

In the late retrograde skarn stage, the representative garnet samples are HG12-28 and HG12-19. These two andradites (Grt IV) show similar features in mineralogy and major element compositions, but are distinct in REE patterns: (1) The former exhibits similar REE patterns as the Grt III rims, with a slightly downward-sloping trend ( $\Sigma\text{REE} = 21.86\text{--}73.32$  ppm, LREE-enriched, HREE-depleted, and  $\Sigma\text{LREE}/\Sigma\text{HREE} = 2.34\text{--}7.46$ ) and moderately negative Eu anomalies ( $\delta\text{Eu} = 0.07\text{--}0.44$ ) (Figure 15d). (2) The latter shows an obviously downward-sloping trend and weak Eu anomalies, and the  $\Sigma\text{LREE}/\Sigma\text{HREE}$  and  $\delta\text{Eu}$  decrease from the core to the rim (core:  $\Sigma\text{REE} = 126.46\text{--}572.19$  ppm,  $\Sigma\text{LREE}/\Sigma\text{HREE} = 494.43$ ,  $\delta\text{Eu} = 2.21$ ; rim:  $\Sigma\text{REE} = 23.52\text{--}593.09$  ppm,  $\Sigma\text{LREE}/\Sigma\text{HREE} = 2.66\text{--}37.67$ ,  $\delta\text{Eu} = 0.49\text{--}0.64$ ) (Figure 15e).

## 5. Discussion

### 5.1. Fluorine and the Formation of Garnet

The EPMA analyses of this study indicate that garnets from the Huanggang deposit contain high concentrations of F, with the garnets from the late prograde skarn stage containing the highest concentrations of F (Figure 10a). Fluorine forms more stable complexes with Si and Al than with Cl or other halogens [42]. Experimental research indicates that aqueous fluids containing 2 ppm F can dissolve 1.5 times more Al from the dissolution of Al silicates than in pure water at 400 °C and 500 bar environments. These data indicate that F can strongly increase the solubility of Al, suggesting in turn that high-salinity and high-F fluids can promote the formation of complexes such as  $\text{NaAl}(\text{OH})_2\text{F}_2$  at higher temperature [42].

Fluid inclusions within the garnets of the Huanggang deposit provide evidence that the fluid from the skarn stage had temperatures ranging from 397 °C to 618 °C, with salinities of 46.84–69.63 wt.% at the lithostatic fluid of 500 bar [43]. This suggests that the formation of garnets was the result of high-F activities facilitating the concentration of Al within magmatic-hydrothermal fluids, thereby generating the F concentrations decreases with decreasing Al within the garnets from the prograde skarn stage to the retrograde skarn stage (Figure 10b). This interpretation is supported by the andradite (Grt IV, sample HG12-28) from the late retrograde skarn stage intergrown with the fluorites (Figure 4f). Moreover, the fluid inclusion evidence suggests that the F concentrations within the fluid are high at the skarn stage of the Huanggang deposit [44]. In general, the high concentrations of F within these garnets also suggest that the magmatic-hydrothermal fluids associated with this stage of skarn formation had high F activities.

### 5.2. Mechanisms in Garnet Substitution

The general chemical formula of garnet is  $\text{X}_3\text{Y}_2\text{Z}_3\text{O}_{12}$ , where X is divalent cations (Ca, Mg, Mn, or  $\text{Fe}^{2+}$ ) in eight-fold coordination, Y is trivalent cations ( $\text{Fe}^{3+}$ , Al, and Cr) in octahedral coordination, and Z is dominantly Si in tetrahedral coordination [22]. Previous research indicates that there are at least four main mechanisms that can explain incorporation of trace elements into garnet crystals: surface adsorption, occlusion, substitution, and interstitial solid solution [45]. The former two of these are controlled by kinetic effects; the latter two are constrained by crystal chemistry [1].

The incorporation of REE, U, and Y into garnet is only possible by replacement of  $\text{X}^{2+}$  cations such as  $\text{Ca}^{2+}$  in the dodecahedral position on the basis of ionic radius [1,3,10]. For  $\text{Eu}^{2+}$ , the substitution is isovalent and does not imply any charge imbalance (i.e., Equation (1)).

In contrast, for REE, U, and Y, coupled substitution is needed to electrically neutralize the structure (i.e., Equation (2)).



The garnets within the Huanggang deposit contain low Na concentrations (Table S2), indicating that these garnets did not undergo  $\text{Na}^+$ - $\text{REE}^{3+}$  coupled substitution. The LA-ICP-MS data show a strong negative correlation between Al and  $\Sigma\text{REE}$  concentrations, and a positive correlation between  $X_{\text{adr}}^{\text{gt}}$  and  $\Sigma\text{REE}$  in garnets of the prograde skarn stage (Figure 12a,b). In addition, our data did not display linear relationships between U, Y, and  $\Sigma\text{REE}$  concentrations in garnets of the retrograde skarn stage (Figure 13a,b), suggesting that the incorporation of those trace elements did not follow the isovalent and coupled substitution mechanisms.

### 5.3. Evolution of Skarn Hydrothermal Fluids

#### 5.3.1. Constraints on Physical–Chemical Conditions

The incorporation of U into garnet is only possible by coupled substituting  $\text{Ca}^{2+}$  in the dodecahedral site and  $\text{Fe}^{3+}$  in the tetrahedral site [1,3,10,46]. Meanwhile,  $\text{U}^{4+}$  is more likely to substitute into garnet than  $\text{U}^{6+}$  [3]. Thus, the U variations in different parts of the garnet crystals can indicate the relative oxygen fugacity of hydrothermal fluids during the garnet formation. Decreasing  $f\text{O}_2$  of the fluid system could reduce U solubility and in turn increase U incorporation into garnets [3,22]. Zhai et al. [21] demonstrated that the core formation of garnets shows low U concentrations in oxidizing conditions with a relatively higher  $f\text{O}_2$  value. Meanwhile, U and Y concentrations in garnets of different hydrothermal stages were plotted in distinct zones (Figure 13a,b), suggesting that garnets of prograde skarn stages principally display relatively low U concentrations, whereas retrograde skarn stages show relatively high U concentrations. Therefore,  $f\text{O}_2$  during the prograde skarn stages was likely to be higher than that of the retrograde skarn stages, which is consistent with the presence of magnetite and hematite in the retrograde skarn stage (Figure 4c) [45,47].

Bau (1991) demonstrated that pH has a major effect on REE fractionation. In general, the REE patterns of the fluid are relatively HREE-enriched and LREE-depleted with negative or no Eu anomaly under nearly neutral conditions [48]. However, numerous studies also demonstrate that  $\text{Cl}^-$  is an efficient transporter for  $\text{Eu}^{2+}$  and a poor carrier for  $\text{REE}^{3+}$  [1]. Allen and Seyfried [49] have studied the influence of  $\text{Cl}^-$  on REE solubility and found that  $\text{Cl}^-$  enhances the stability of soluble  $\text{Eu}^{2+}$ . Thus, the negative Eu anomalies in the late prograde and early retrograde stages might be explained by the absence of complex agents such as  $\text{Cl}^-$  [22]. However, the  $\text{Cl}^-$  concentrations in fluid inclusions trapped in Huanggang garnet range from 1.57 to 62.77  $\mu\text{g/g}$  [50]. Therefore, based on the chondrite-normalized REE patterns of garnets from Huanggang deposit, garnets show distinctly negative Eu anomalies (Figure 15a–d), which suggests that the garnets from the skarn stages mainly formed from nearly neutral pH fluid. In contrast, the distinctly positive Eu anomalies (Figure 15e) in andradite cores (HG12-19) from the late retrograde skarn stage imply their crystallization in mildly acidic conditions.

#### 5.3.2. Constraints on Fluid–Rock Interaction

The distribution coefficient of trace elements (Y, Zr, and Sc) in the hydrothermal fluid decreases with increasing fluid/rock ratio [1], which reflects the original and developed fluid or the influence of an external fluid [11]. Furthermore, the change in  $\Sigma\text{REE}$  is associated with the entry of externally buffered fluid into the metallogenic system [3]. Al-rich garnets from the Crown Jewel deposit form by diffusive metasomatism at low W/R ratios, whereas Fe-rich garnets grow rapidly by advective metasomatism at higher W/R ratios [1], which may be related to different hydrothermal fluid composition and metamorphic processes [10,21].

The andradite (Grt I) is characterized by isotropic, LREE-enriched, and HREE-depleted patterns, whereas the grossular (Grt II) is characterized by euhedral crystal and obvious twinning, LREE-depleted, and HREE-enriched patterns (Figures 5c and 15a,b), which suggests that the former (Grt I) is originated from magmatic-derived fluids, requiring rapid growth by infiltration metasomatism at high W/R ratios, and the latter (Grt II) from a relatively HREE-enriched melt/fluid, and requires slow crystal growth by diffusive metasomatism at low water/rock (W/R) ratios from host-rock buffered metasomatic fluid compositions [1], whereas the Fe<sup>3+</sup>-rich andradite (Grt III) is present as a veinlet (Figure 5c) that is indicative of rapid growth by infiltration metasomatism at high W/R ratios from magmatic-derived fluids [1,22]. At the prograde skarn stage, a host-rock buffered metasomatic fluid with a relatively low REE concentration was derived from the marble or andesite. The grossulars (Grt II), which had a low REE concentration but enriched in HREE, deposited under relatively low W/R ratios in a nearly closed system from host-rock-derived fluids by a process of diffusion metasomatism. An increase in W/R ratio and continuing infiltration metasomatism promoted incorporation of REE, especially LREE, into Fe<sup>3+</sup>-rich andradite (Grt III) core [21].

As previously discussed, Fe<sup>3+</sup>-rich andradite (Grt III) from the early retrograde skarn stage is characterized by dodecahedral {110} forms with LREE-depleted and HREE-enriched patterns (Figures 5e,f and 15c), indicative of slow crystal growth by diffusive metasomatism at low W/R ratios [3,51]. In comparison, the development of trapezohedron {211} faces on the rim of Fe<sup>3+</sup>-rich andradite (Grt III) with LREE-enriched and HREE-depleted patterns (Figures 5e,f and 15c) requires rapid growth by infiltration metasomatism at high W/R ratios [3,49]. The prograde skarn stage had the high W/R ratios and strong infiltration metasomatism, which led to the Fe<sup>3+</sup>-rich garnets having high REE concentration. Continuous crystallization resulted in a decrease in REE concentration in the residual fluid, so that andradite (Grt IV) has lower  $\Sigma$ REE than the Fe-rich garnet (Grt III) [21]. Thus, at the retrograde skarn stage, the water–rock reaction declined.

#### 5.4. Mechanisms of W–Sn–Mo Mineralization

All garnet types in the Huanggang deposit contain certain amounts of W, Sn, and Mo, and especially the garnets GrtIII and GrtIV, which contain the highest amounts of W (24.8–1237.26 ppm), Sn (186.30–6357.70 ppm), and Mo (0.1–8.44 ppm). The great enrichment in W, Sn, and Mo was closely related to the early retrograde stage of fluid flow that had the highest flux. The highest flux implies a high-*f*O<sub>2</sub> condition responsible for the incorporation of these elements' formations. On the basis of Figure 14, W and Mo concentration change has to do with contents of andradite in garnet. Due to the highest andradite contents in the retrograde skarn stage, it is most likely that the iron content in garnet (andradite) favors this metal element's enrichment, which also suggests that it is formed in high-*f*O<sub>2</sub> condition. Another piece of evidence is that, although W- or Mo-bearing minerals (e.g., scheelite and molybdenite) are not observed in the retrograde skarn stage, it is possible that their contents are not sufficient to cause W or Mo precipitation, but there is a large amount of magnetite precipitation in this stage (Figure 4c). The occurrence of magnetite suggests a relatively high-*f*O<sub>2</sub> condition, which favors the incorporation of W and Mo.

Existing data on the incorporation of tin into the structure of garnet indicate that it occurs as Sn<sup>4+</sup> substituting for Fe<sup>3+</sup> within the octahedral site [52,53]. W and Mo substitutions are similar, but they are considered to be hexavalent within the octahedral site [54,55]. In general, the positive correlation between W or Mo concentrations and the andradite component in the garnets of the Huanggang deposit (Figure 14a,c) suggests that an increase in the Fe content is favorable for W and Mo substitutions. Remarkably, similar positive correlations between  $\delta$ Eu and W or Mo (Figure 14b,d) indicate that an increase in the  $\delta$ Eu ratio can also promote the substitutions of these metal elements. There is no linear relationship between  $\delta$ Eu, andradite, and Sn (Figure 14e,f), which suggests that they are at least not controlled by fluid chemistry, and perhaps the precipitation of cassiterite has nothing to do with the garnets of skarn stage.

### 5.5. Formation and Evolution of Garnets from Huanggang Skarn Deposit

Formation of skarn is involving different hydrothermal stages and a continuous fluid evolution process [56]. Zonation in skarns generally follows the predictions of metasomatic zoning theory and reflects changes in fluid dynamics (diffusion or infiltration), fluid physical–chemical condition (pH and  $fO_2$ ), temperature, pressure, and host rock composition [1,57–59]. Our findings in this study provide insights into the mobilization of major elements, trace elements, and REEs, and their influence on the composition of garnets in various skarn stages and the subsequent evolution of the garnet (Figure 16).

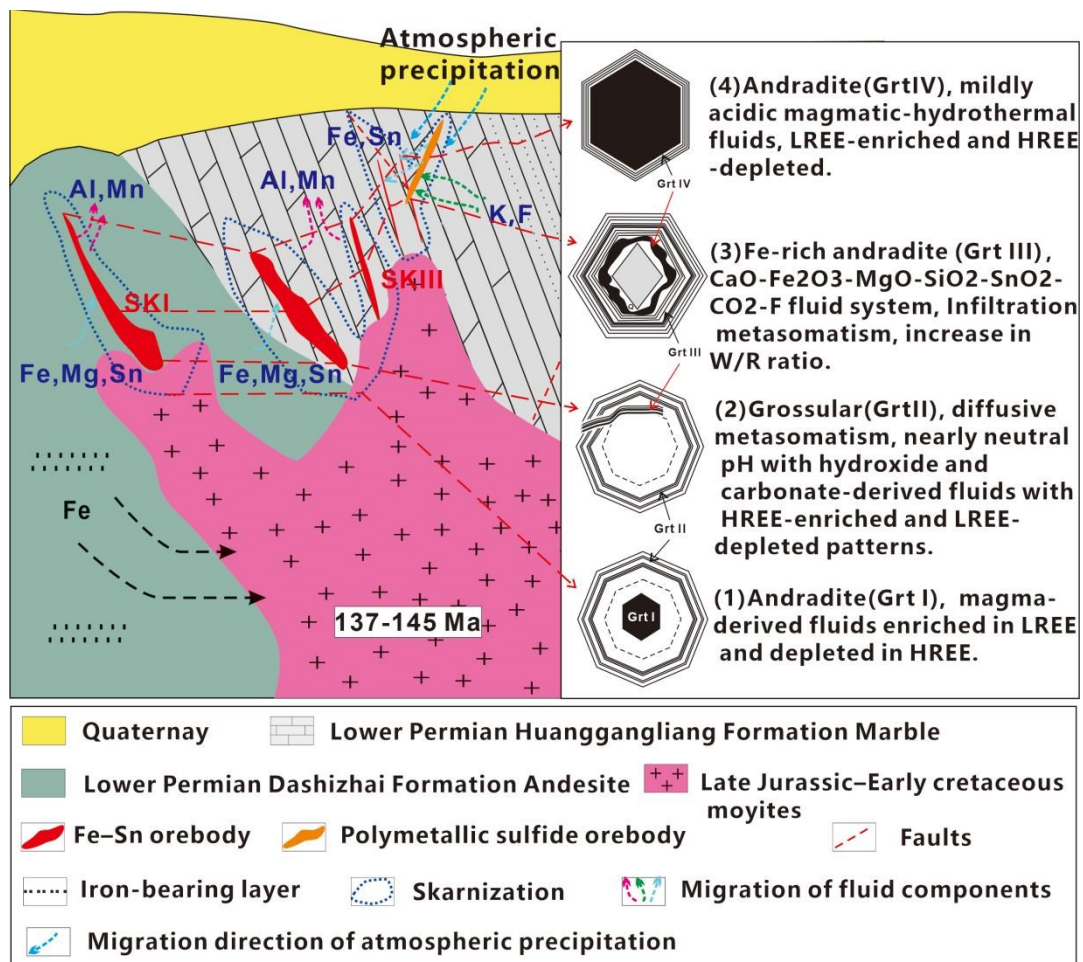


**Figure 16.** Model of the formation processes and fluid evolution for the garnet in the Huanggang deposit.

At the beginning of the prograde skarn stage, magma-derived fluids enriched in LREE and depleted in HREE interacted with surrounding marble to produce skarn minerals (e.g., andradite Grt I, Figure 15a). The prograde stage was formed from a CaO-Al<sub>2</sub>O<sub>3</sub>-SiO<sub>2</sub>-MnO fluid system (Figures 8a,b and 9a,b), and characterized by the development of minerals such as grossular (Grt II), hedenbergite, vesuvianite, quartz, and calcite. The absence of oscillatory zoning in Grt I and Grt II core indicates that the grossular crystallized at a relatively stable and closed system by diffusive metasomatism [23], which is consistent with the correlation between Y and total REEs [24] (Figure 13b). Diffusive metasomatism will produce fluids and alteration products in which REE composition is buffered by the composition of the host rocks, due to long pore fluid residence under closed-system conditions. These fluids have nearly neutral pH, with hydroxide and carbonate as the main complexing agents [23,24]. Thus, the grossular from the prograde skarn stage exhibits HREE-enriched and LREE-depleted patterns with obviously negative Eu anomalies (Figures 15b and 16).

With an increase in iron-rich mineral compositions, many skarns follow a characteristic evolutionary trend in space and time, from more diffusive metasomatism to more infiltration metasomatism [56–58]. The diffusive metasomatism changing to infiltration metasomatism is indicated by an increase in Fe<sup>3+</sup>-rich andradite (Grt III) and andradite (Grt IV). The retrograde skarn stage was formed from a CaO-Fe<sub>2</sub>O<sub>3</sub>-MgO-SiO<sub>2</sub>-SnO<sub>2</sub>-W-CO<sub>2</sub>-F fluid system (Figures 8c,d and 9c–e), and characterized by the development of minerals such as magnetite, cassiterite, scheelite, andradite (Grt III, Grt IV), diopside, calcite, fluorite, and quartz. The presence of oscillatory zoning and many fractures showed that the garnets were likely formed under an oscillatory physicochemical and open system condition by infiltration metasomatism [23], which is consistent with the lack of correlation between Y and total REEs (Figure 13b) [21]. Infiltration metasomatism, associated with an increase in W/R ratio, would produce fluids and mineral assemblages buffered by mildly acidic magmatic-hydrothermal fluids with chloride complexes that can be important in Eu<sup>2+</sup> transport [1]. Thus, the andradite core (Grt IV) from the retrograde skarn stage has LREE-enriched and HREE-depleted patterns with weakly positive Eu anomalies (Figures 15e and 16).

## 6. Conclusions

1. Garnets at Huanggang deposit can be divided into four types of garnets from the prograde skarn stage (Grt I, GrtII) to the retrograde skarn stage (Grt III, GrtIV).
2. The in situ LA-ICP-MS analytical results of garnets in the prograde skarn stage reveal that andradite cores (Grt I) were formed from a fluid that was generally LREE-rich, with relatively high  $\Sigma$ REE, high LREE/HREE ratios, and weak negative Eu anomalies, whereas grossular rims (Grt II) were crystallized from a fluid that was typically HREE-rich, with relatively low  $\Sigma$ REE, low LREE/HREE ratios, and obviously negative Eu anomalies.
3. The in situ LA-ICP-MS analytical results of garnets in the retrograde skarn stage demonstrate that Fe<sup>3+</sup>-rich andradite cores (Grt III) have a flat trend with high  $\Sigma$ REE and obvious negative Eu anomalies, whereas andradite rims (Grt IV) were formed from a fluid with relatively low  $\Sigma$ REE, HREE-rich, and obviously negative Eu anomalies.
4. The garnets from the prograde skarn stage (Grt I–II) principally display relatively lower U and higher Y concentrations than those from the retrograde skarn stage (Grt III–IV). From prograde skarn stage to retrograde skarn stage, the garnet formation environment changed from near-neutral pH, oxidizing conditions, and high W/R ratios to acidic, reducing conditions and low W/R ratios, which implies that compositional and/or physicochemical changes in fluid may contribute a major influence on incorporating trace elements and REEs into garnet crystals.

**Supplementary Materials:** The following supporting information can be downloaded at: <https://www.mdpi.com/article/10.3390/min13030450/s1>. In situ LA-ICP-MS of zoned garnets from the Huanggang skarn iron–tin polymetallic deposit, Southeastern Mongolia, Northern China, Table S1: EMPA geochemical data (wt.%) of the Huanggang garnets; Table S2: LA-ICP-MS trace and rare earth elements data of the Huanggang garnets.

**Author Contributions:** Conceptualization, B.R.; investigation, H.L.; writing—original draft, writing—review and editing, W.M. All authors have read and agreed to the published version of the manuscript.

**Funding:** This research was funded by the China Geological Survey (grant number, DD20160101), the National Key Research and Development Plan (2022YFC2903501-02), and the National Natural Science Foundation of China (grant 41802101).

**Data Availability Statement:** Not applicable.

**Acknowledgments:** The authors would like to thank Xiejun Fan and the managers of the Inner Mongolia Huanggang Mining Limited Liability Company for their support of our fieldwork. Two anonymous reviewers are gratefully acknowledged for their constructive and valuable comments.

**Conflicts of Interest:** The authors declare no conflict of interest.

## References

1. Gaspar, M.; Knaack, C.; Meinert, L.D.; Moretti, R. REE in skarn systems: A LA-ICP-MS study of garnets from the Crown Jewel gold deposit. *Geochim. Cosmochim. Acta* **2008**, *72*, 185–205. [\[CrossRef\]](#)
2. Peng, H.; Zhang, C.; Mao, J.; Santosh, M.; Zhou, Y.; Hou, L. Garnets in porphyry–skarn systems: A LA-ICP-MS, fluid inclusion, and stable isotope study of garnets from the Hongniu–Hongshan copper deposit, Zhongdian area, NW Yunnan Province, China. *J. Asian Earth Sci.* **2015**, *103*, 229–251. [\[CrossRef\]](#)
3. Smith, M.P.; Henderson, P.; Jeffries, T.; Long, J.; Williams, C.T. The rare earth elements and uranium in garnets from the Beinn an Dubhaich aureole, Skye, Scotland, UK: Constraints on processes in a dynamic hydrothermal system. *J. Petrol.* **2004**, *45*, 457–484. [\[CrossRef\]](#)
4. Cheng, H.; Zhang, C.; Vervoort, J.D.; Lu, H.; Wang, C.; Cao, D. Zircon U–Pb and garnet Lu–Hf geochronology of eclogites from the Lhasa Block of northern Tibet. *Lithos* **2012**, *155*, 341–359. [\[CrossRef\]](#)
5. Scherer, E.E.; Cameron, K.L.; Blichert-Toft, J. Lu–Hf garnet geochronology: Closure temperature relative to the Sm–Nd system and the effects of trace mineral inclusions. *Geochim. Cosmochim. Acta* **2000**, *64*, 3413–3432. [\[CrossRef\]](#)
6. Schmidt, A.; Mezger, K.; O'Brien, P.J. The time of eclogite formation in the ultrahigh pressure rocks of the Sulu terrane: Constraints from Lu–Hf garnet geochronology. *Lithos* **2011**, *125*, 743–756. [\[CrossRef\]](#)
7. Fernando, G.W.A.R.; Hauzenberger, C.A.; Baumgartner, L.P.; Hofmeister, W. Modeling of retrograde diffusion zoning in garnet: Evidence for slow cooling of granulites from the Highland Complex of Sri Lanka. *Mineral. Petrol.* **2003**, *78*, 53–71. [\[CrossRef\]](#)
8. Kim, H.S. Deformation-induced garnet zoning. *Gondwana Res.* **2006**, *10*, 379–388. [\[CrossRef\]](#)
9. Martin, L.; Balleve, M.; Boulvais, P.; Halfpenny, A.; Vanderhaeghe, O.; Duch E Ne, S.E.P.; Deloule, E. Garnet re-equilibration by coupled dissolution—Reprecipitation: Evidence from textural, major element and oxygen isotope zoning of ‘cloudy’ garnet. *J. Metamorph. Geol.* **2011**, *29*, 213–231. [\[CrossRef\]](#)
10. Dziggel, A.; Wulff, K.; Kolb, J.; Meyer, F.M.; Lahaye, Y. Significance of oscillatory and bell-shaped growth zoning in hydrothermal garnet: Evidence from the Navachab gold deposit. *Namibia. Chem. Geol.* **2009**, *262*, 262–276. [\[CrossRef\]](#)
11. Jamtveit, B.; Wogelius, R.A.; Fraser, D.G. Zonation patterns of skarn garnets—records of hydrothermal system evolution. *Geology* **1993**, *21*, 113–116. [\[CrossRef\]](#)
12. Ginibre, C.; Worner, G. Variable parent magmas and recharge regimes of the Parinacota magma system (N. Chile) revealed by Fe, Mg and Sr zoning in plagioclase. *Lithos* **2007**, *98*, 118–140. [\[CrossRef\]](#)
13. Sharygin, V.V.; Sobolev, N.V.; Channer, D.M.D. Oscillatory-zoned crystals of pyrochlore-group minerals from the Guaniamo kimberlites, Venezuela. *Lithos* **2009**, *112*, 976–985. [\[CrossRef\]](#)
14. Streck, M.J. Mineral Textures and Zoning as Evidence for Open System Processes. *Rev. Mineral. Geochem.* **2008**, *69*, 595–622. [\[CrossRef\]](#)
15. Chakraborty, S. Compositional Zoning and Cation Diffusion in Garnets. *Diffus. At. Ordering Mass Transp. Sel. Top. Geochem. Adv. Phys. Geochem.* **1991**, *8*, 120–175.
16. Hickmott, D.D.; Shimizu, N.; Spear, F.S.; Selverstone, J. Trace-element zoning in a metamorphic garnet. *Geology* **1987**, *15*, 573–576. [\[CrossRef\]](#)
17. Buick, I.S.; Hermann, J.; Williams, I.S.; Gibson, R.L.; Rubatto, D. A SHRIMP U–Pb and LA-ICP-MS trace element study of the petrogenesis of garnet-cordierite-orthoamphibole gneisses from the Central Zone of the Limpopo Belt, South Africa. *Lithos* **2006**, *88*, 150–172. [\[CrossRef\]](#)
18. Whitney, D.L. Garnets as open systems during regional metamorphism. *Geology* **1996**, *24*, 147–150. [\[CrossRef\]](#)
19. Cutts, K.A.; Kinny, P.D.; Strachan, R.A.; Hand, M.; Leslie, A.G. Three metamorphic events recorded in a single garnet: Integrated phase modelling, in situ la-icpms and sims geochronology from the moine supergroup, NW Scotland. *J. Metamorph. Geol.* **2010**, *28*, 249–267. [\[CrossRef\]](#)
20. Xiao, X.; Zhou, T.; White, N.C.; Zhang, L.; Fan, Y.; Wang, F.; Chen, X. The formation and trace elements of garnet in the skarn zone from the Xinqiao Cu–S–Fe–Au deposit, Tongling ore district, Anhui Province, Eastern China. *Lithos* **2018**, *302*, 467–479. [\[CrossRef\]](#)
21. Zhai, D.; Liu, J.; Zhang, H.; Wang, J.; Su, L.; Yang, X.; Wu, S. Origin of oscillatory zoned garnets from the Xieertala Fe–Zn skarn deposit, northern China: In situ LA-ICP-MS evidence. *Lithos* **2014**, *190*, 279–291. [\[CrossRef\]](#)
22. Zhang, Y.; Shao, Y.; Wu, C.; Chen, H. LA-ICP-MS trace element geochemistry of garnets: Constraints on hydrothermal fluid evolution and genesis of the Xinqiao Cu–S–Fe–Au deposit, eastern China. *Ore Geol. Rev.* **2017**, *86*, 426–439. [\[CrossRef\]](#)
23. Zhou, Z.H.; Mao, J.W.; Lyckberg, P. Geochronology and isotopic geochemistry of the A-type granites from the Huanggang Sn–Fe deposit, southern Great Hinggan Range, NE China: Implication for their origin and tectonic setting. *J. Asian Earth Sci.* **2012**, *49*, 272–286. [\[CrossRef\]](#)
24. Mei, W.; Lv, X.; Liu, Z.; Tang, R.; Ai, Z.; Wang, X.; Cisse, M. Geochronological and geochemical constraints on the ore-related granites in Huanggang deposit, Southern Great Xing’an Range, NE China and its tectonic significance. *Geosci. J.* **2015**, *19*, 53–67. [\[CrossRef\]](#)
25. Zhai, D.; Liu, J.; Zhang, H.; Yao, M.; Wang, J.; Yang, Y. S–Pb isotopic geochemistry, U–Pb and Re–Os geochronology of the Huanggangliang Fe–Sn deposit, Inner Mongolia, NE China. *Ore Geol. Rev.* **2014**, *59*, 109–122. [\[CrossRef\]](#)
26. Mei, W.; Lv, X.; Cao, X.; Liu, Z.; Zhao, Y.; Ai, Z.; Tang, R.; Abfaua, M.M. Ore genesis and hydrothermal evolution of the Huanggang skarn iron–tin polymetallic deposit, southern Great Xing’an Range: Evidence from fluid inclusions and isotope analyses. *Ore Geol. Rev.* **2015**, *64*, 239–252. [\[CrossRef\]](#)

27. Wang, C.; Shao, Y.J.; Zhang, X.; Dick, J.; Liu, Z.F. Trace element geochemistry of magnetite: Implications for ore genesis of the Huanggangliang Sn-Fe deposit, Inner Mongolia, Northeastern China. *Minerals* **2018**, *8*, 195. [[CrossRef](#)]
28. Zhou, Z.H.; Liu, H.W.; Chang, G.X.; Lv, L.S.; Li, T.; Yang, Y.J.; Zhang, R.J.; Ji, X.H. Mineralogical characteristics of skarns in the Huanggang Sn-Fe deposit of Inner Mongolia and their metallogenic indicating significance. *Acta Petrol. Mineral.* **2011**, *30*, 97–112. (In Chinese with English Abstract)
29. Xiao, W.; Windley, B.F.; Hao, J.; Zhai, M. Accretion leading to collision and the Permian Solonker suture, Inner Mongolia, China: Termination of the central Asian orogenic belt. *Tectonics* **2003**, *22*, 1069–1088. [[CrossRef](#)]
30. Wu, F.Y.; Sun, D.Y.; Ge, W.C.; Zhang, Y.B.; Grant, M.L.; Wilde, S.A.; Jahn, B.M. Geochronology of the Phanerozoic granitoids in northeastern China. *J. Asian Earth Sci.* **2011**, *41*, 1–30. [[CrossRef](#)]
31. Liu, C.; Bagas, L.; Wang, F. Isotopic analysis of the super-large Shuangjianzishan Pb–Zn–Ag deposit in Inner Mongolia, China: Constraints on magmatism, metallogenesis, and tectonic setting. *Ore Geol. Rev.* **2016**, *75*, 252–267. [[CrossRef](#)]
32. Ouyang, H.; Mao, J.; Santosh, M.; Zhou, J.; Zhou, Z.; Wu, Y.; Hou, L. Geodynamic setting of Mesozoic magmatism in NE China and surrounding regions: Perspectives from spatio-temporal distribution patterns of ore deposits. *J. Asian Earth Sci.* **2013**, *78*, 222–236. [[CrossRef](#)]
33. Ouyang, H.; Mao, J.; Zhou, Z.; Su, H. Late Mesozoic metallogeny and intracontinental magmatism, southern Great Xing’an Range, northeastern China. *Gondwana Res.* **2015**, *27*, 1153–1172. [[CrossRef](#)]
34. Liu, J.M.; Zhang, R.; Zhang, Q.Z. The regional metallogeny of Da Hinggan Ling, China. *Earth Sci. Front.* **2004**, *11*, 269–277. (In Chinese with English abstract)
35. IMGT (Inner Mongolia No. 3 Geological Team). Exploration Report on the Huanggang Fe–Sn Ore Deposit, Keshiketengqi, Inner Mongolia Autonomous Region. 1983. (In Chinese)
36. Liu, Y.; Hu, Z.; Gao, S.; Gunther, D.; Xu, J.; Gao, C.; Chen, H. In situ analysis of major and trace elements of anhydrous minerals by LA-ICP-MS without applying an internal standard. *Chem. Geol.* **2008**, *257*, 34–43. [[CrossRef](#)]
37. Einaudi, M.T. Skarn deposits. *Econ. Geol.* **1981**, *75*, 317–391.
38. Meinert, L.D. Skarns and skarn deposits. *Geosci. Can.* **1992**, *19*, 145–162.
39. Meinert, L.D. Application of skarn deposit zonation models to mineral exploration. *Explor. Min. Geol.* **1997**, *6*, 185–208.
40. Sun, S.S.; McDonough, W.F. Chemical and isotopic systematics of oceanic basalts: Implications for mantle composition and processes. *Geol. Soc.* **1989**, *42*, 313–345. [[CrossRef](#)]
41. McDonough, W.F.; Sun, S.S. The composition of the Earth. *Chem. Geol.* **1995**, *120*, 223–253. [[CrossRef](#)]
42. Tagirov, B.; Schott, J.; Harrichoury, J.C. Experimental study of aluminum–fluoride complexation in near-neutral and alkaline solutions to 300 °C. *Chem. Geol.* **2002**, *184*, 301–310. [[CrossRef](#)]
43. Bai, D.M.; Fu, G.L.; Nie, F.J.; Jiang, S.H.; Liu, Y.F. Integrated ore-prospecting model for the skarn polymetallic deposit in Southeastern Inner Mongolia. *J. Jilin Univ.* **2011**, *41*, 1968–1976. (In Chinese with English abstract).
44. Wang, L.J.; Wang, J.B.; Wang, Y.W.; Mao, Q. Fluid-melt Inclusions in Fluorite of the Huanggangliang Skarn Iron-Tin Deposit and Their Significance to Mineralization. *Acta Geol. Sin.* **2001**, *75*, 204–211.
45. Mcintire, W.L. Trace element partition coefficients—A review of theory and applications to geology. *Geochim. Cosmochim. Acta* **1963**, *27*, 1209–1264. [[CrossRef](#)]
46. Grew, E.S.; Locock, A.J.; Mills, S.J.; Galuskina, I.O.; Galuskin, E.V. Nomenclature of the garnet supergroup. *Am. Mineral.* **2013**, *98*, 785–810. [[CrossRef](#)]
47. Mei, W.; Lv, X.; Wang, X.D. Alteration, Mineralization and Genesis of Huanggang Skarn Iron-Tin Polymetallic Deposit, Southern Great Xing’an Range. *Earth Sci.* **2020**, *45*, 4428–4445. (In Chinese with English Abstract)
48. Bau, M. Rare-earth element mobility during hydrothermal and metamorphic fluid-rock interaction and the significance of the oxidation state of europium. *Chem. Geol.* **1991**, *93*, 219–230. [[CrossRef](#)]
49. Allen, D.E.; Seyfried, W.E. REE controls in ultramafic hosted MOR hydrothermal systems: An experimental study at elevated temperature and pressure. *Geochim. Cosmochim. Acta* **2005**, *69*, 675–683. [[CrossRef](#)]
50. Zhou, Z.H.; Wang, A.S.; Li, T. Fluid inclusion characteristics and metallogenic mechanism of Huanggang Sn–Fe deposit in Inner Mongolia. *Miner. Depos.* **2011**, *30*, 867–889. (In Chinese with English Abstract)
51. Jamtveit, B.; Hervig, R.L. Constraints on transport and kinetics in hydrothermal systems from zoned garnet crystals. *Science* **1994**, *263*, 505–508. [[CrossRef](#)]
52. Chen, J.; Halls, C.; Stanley, C.J. Tin-bearing skarns of South China: Geological setting and mineralogy. *Ore Geol. Rev.* **1992**, *7*, 225–248. [[CrossRef](#)]
53. Zhou, J.; Feng, C.; Li, D. Geochemistry of the garnets in the Baiganhu W–Sn orefield, NW China. *Ore Geol. Rev.* **2017**, *82*, 70–92. [[CrossRef](#)]
54. Dhivya, L.; Janani, N.; Palanivel, B.; Murugan, R. Li<sup>+</sup> transport properties of W substituted Li<sub>7</sub>La<sub>3</sub>Zr<sub>2</sub>O<sub>12</sub> cubic lithium garnets. *AIP Adv.* **2013**, *3*, 082115. [[CrossRef](#)]
55. Liu, X.; Li, L.; Noh, H.M.; Moon, B.K.; Choi, B.C.; Jeong, J.H. Chemical bond properties and charge transfer bands of O<sup>2−</sup>–Eu<sup>3+</sup>, O<sup>2−</sup>–Mo<sup>6+</sup> and O<sup>2−</sup>–W<sup>6+</sup> in Eu<sup>3+</sup>-doped garnet hosts Ln<sub>3</sub>M<sub>5</sub>O<sub>12</sub> and ABO<sub>4</sub> molybdate and tungstate phosphors. *Dalton Trans.* **2014**, *43*, 8814. [[CrossRef](#)] [[PubMed](#)]
56. Meinert, L.D.; Dipple, G.M.; Nicolescu, S. World skarn deposits. In *Economic Geology 100th Anniversary Volume*; Society of Economic Geologists: Littleton, CO, USA, 2005; pp. 299–336.

57. Ruan, C.T.; Yu, X.Y.; Su, S.G.; Santosh, M.; Qin, L.J. Anatomy of Garnet from the Nanminghe Skarn Iron Deposit, China: Implications for Ore Genesis. *Minerals* **2022**, *12*, 845. [[CrossRef](#)]
58. Yu, F.; Shu, Q.H.; Niu, X.D.; Xing, K.; Li, L.L.; David, R.L.; Zeng, Q.W.; Yang, W.J. Composition of Garnet from the Xianghualing Skarn Sn Deposit, South China: Its Petrogenetic Significance and Exploration Potential. *Minerals* **2020**, *10*, 456. [[CrossRef](#)]
59. Tan, F.C.; Kong, H.; Liu, B.; Wu, Q.H.; Chen, S. In Situ U-Pb Dating and Trace Element Analysis of Garnet in the Tongshanling Cu Polymetallic Deposit, South China. *Minerals* **2023**, *13*, 187. [[CrossRef](#)]

**Disclaimer/Publisher's Note:** The statements, opinions and data contained in all publications are solely those of the individual author(s) and contributor(s) and not of MDPI and/or the editor(s). MDPI and/or the editor(s) disclaim responsibility for any injury to people or property resulting from any ideas, methods, instructions or products referred to in the content.